Marine and Petroleum Geology 138 (2022) 105522

Contents lists available at ScienceDirect

Marine and Petroleum Geology

journal homepage: www.elsevier.com/locate/marpetgeo

Quantitative characterization of various oil contents and spatial distribution in lacustrine shales: Insight from petroleum compositional characteristics derived from programed pyrolysis

Ming Guan [a,b,c], Xiaoping Liu [a,b,*], Zhijun Jin [d,e,**], Jin Lai [a,b], Jie Liu [f], Biao Sun [a,b], Tian Liu [a,b], Zuxian Hua [a,b], Wen Xu [a,b], Honglin Shu [g], Gaocheng Wang [g], Mengcai Liu [g], Yufeng Luo [g]

[a] State Key Laboratory of Petroleum Resources and Prospecting, China University of Petroleum (Beijing), Beijing, 102249, China
[b] College of Geosciences, China University of Petroleum (Beijing), Beijing, 102249, China
[c] Research Institute of Petroleum Exploration and Development, China National Petroleum Corporation, Beijing, 100083, China
[d] Institute of Energy, Peking University, Beijing, 100871, China
[e] State Key Laboratory of Shale Oil and Gas Enrichment Mechanisms and Effective Development, Beijing, 100083, China
[f] Sinopec International Petroleum Exploration and Production Corporation, Beijing, 100029, China
[g] Research Institute of Petroleum Exploration Development, PetroChina Zhejiang Oilfield Company, Hangzhou, Zhejiang, China

ARTICLE INFO

Keywords:
Oil content
Lacustrine shale
Pyrolysis S_1
Spatial distribution
Controlling factor

ABSTRACT

The strong heterogeneity of lacustrine shale oil occurrences and the lack of proper parameters representing the shale oil content are impediments to assessing shale oil reserves. The shale oil content was characterized in the study using petroleum compositional characteristics determined by loss light hydrocarbon restoration and chemical kinetics decomposition and reconstruction of hydrocarbon groups; the shale oil spatial occurrence of the Second Mbr of the Funing Fm in Haian Sag, Subei Basin was determined using logging prediction and measured data; and finally, the controlling factors of shale oil content were discussed. Organic matter abundance, thermal maturity, and lithofacies have the primary impact on shale oil content. Shale oil enrichment intervals are distributed in an adjacent part of the maximum flood surface in the third-order sequence and some ascending semi-cycles in the fourth-order sequences in the deep sag area. This work has implications for exploration target optimization and resource potential evaluation of shale oil.

1. Introduction

The success of the North American shale revolution has reshaped the global energy landscape and set off an upsurge of unconventional oil and gas exploration around the world (Han et al., 2021; Soeder, 2018). Unconventional oil and gas resources have shown great promise as a replacement for conventional oil and gas resources (EIA, 2017; Jin et al., 2019; Zou et al., 2019). In recent years, China has made significant progress in the exploration and development of lacustrine shale oil (Li et al., 2020a, 2020b; Wang et al., 2019). The accurate evaluation of shale oil content and the fine portrait of shale oil spatial occurrence are the prerequisites for calculating shale oil reserves and prioritizing exploration targets. However, the relevant research is impeded by the strong heterogeneity of lacustrine shale oil spatial occurrences and a lack of proper parameters representing the shale oil content.

Oil exists primarily in two forms in organic-rich shale: adsorbed in the interior of kerogen and on the surface of hydrophobic kerogen/mineral particles, and free in the nanometer to micrometer scale pore-fracture system (Li et al., 2020a, 2020b; Sang et al., 2018; Wang et al., 2015). Oil content is the hydrocarbon content retained in the shale reservoirs (Zhang et al., 2012). It can be qualitatively evaluated through core observation, fluorescence thin-section observation, logging wells, oil production tests, and well completion data; and it can also be quantified by geochemical parameters, experimental analysis, formation energy analysis and calculation, and logging evaluation, etc. Some common shale oil content parameters, such as extractible organic matter (EOM), pyrolysis S_1, and oil saturation, are commonly used to describe the occurrence and enrichment characteristics of shale oil (Nikolaev and

* Corresponding author. College of Geosciences, China University of Petroleum (Beijing), Beijing, 102249, China.
** Corresponding author. Institute of Energy, Peking University, Beijing, 100871, China.
E-mail addresses: liuxiaoping@cup.edu.cn (X. Liu), jinzj1957@pku.edu.cn (Z. Jin).

https://doi.org/10.1016/j.marpetgeo.2021.105522
Received 19 October 2021; Received in revised form 30 December 2021; Accepted 31 December 2021
Available online 4 January 2022

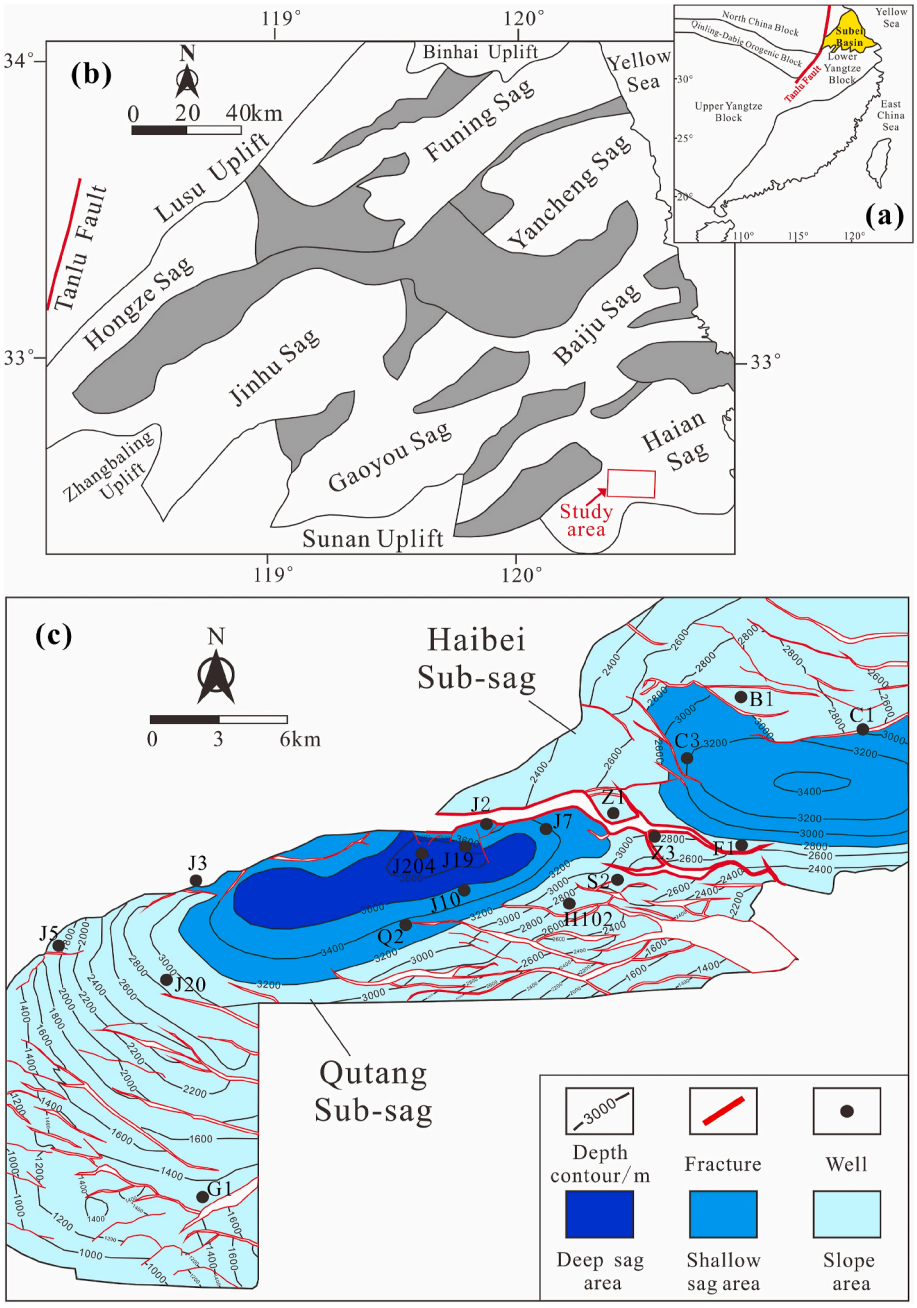

Fig. 1. Map showing the location of Subei Basin and study area: (a) the location of the Subei Basin; (b) tectonic framework of the Subei Basin and the location of the study area (Chen et al., 2009; Shu et al., 2005); and (c) the top surface depth contour map of the Second Mbr of the Funing Fm in the study area (Jiang et al., 2018).

Kazak, 2019), evaluate resource potential, and prioritize favorable intervals. Oil saturation is calculated by the ratio of oil volume to pore volume in samples. For tight reservoirs, it is very difficult to obtain these key parameters to calculate oil saturation, such as oil volume, water volume, porosity, etc. By contrast, the pyrolysis S_1 and EOM are more available. However, the volatilization loss of low-carbon number components is caused by sample pulverization, long-time heating, and evaporation-concentration during the extraction process. The S_1 derived from Rock-Eval may be a more appropriate parameter to present the oil content of lacustrine shale with a high degree of heterogeneity due to its shorter experimental duration, lower cost, and lower sample consumption. Large molecular heavy oil, bitumen, or migrated oils in shale, on the other hand, will result in S_1 "carry-over" and an overestimation of S_2. There are currently two main ways to deal with this problem: one is experimental methods, either that compare pyrolysis results derived from the extracted sample and the original sample, and then quantitatively determine the heavy hydrocarbon components (Jarvie, 2012; Zink et al., 2016), or that change the pyrolysis temperature program to directly detect the heavy hydrocarbon component content (Abrams et al., 2017; Jiang et al., 2016a; Romero-Sarmiento et al., 2016; Romero-Sarmiento, 2019); the other method is to use mathematical methods to decompose and reconstruct various components or products based on the chemical kinetic properties of petroleum components and kerogen in shales (Chen et al., 2018a; Li et al., 2018, 2020c). Furthermore, the loss of gaseous and light hydrocarbons can reach C_{10}, even C_{15}, during the drilling and coring, storage, and sample pretreatment processes (Jiang et al., 2016b; Michael et al., 2013). Therefore, the restoration of gaseous and light hydrocarbons is a must for using these parameters to characterize shale oil content. Although a series of methods have been used to explore the restoration of gaseous and light

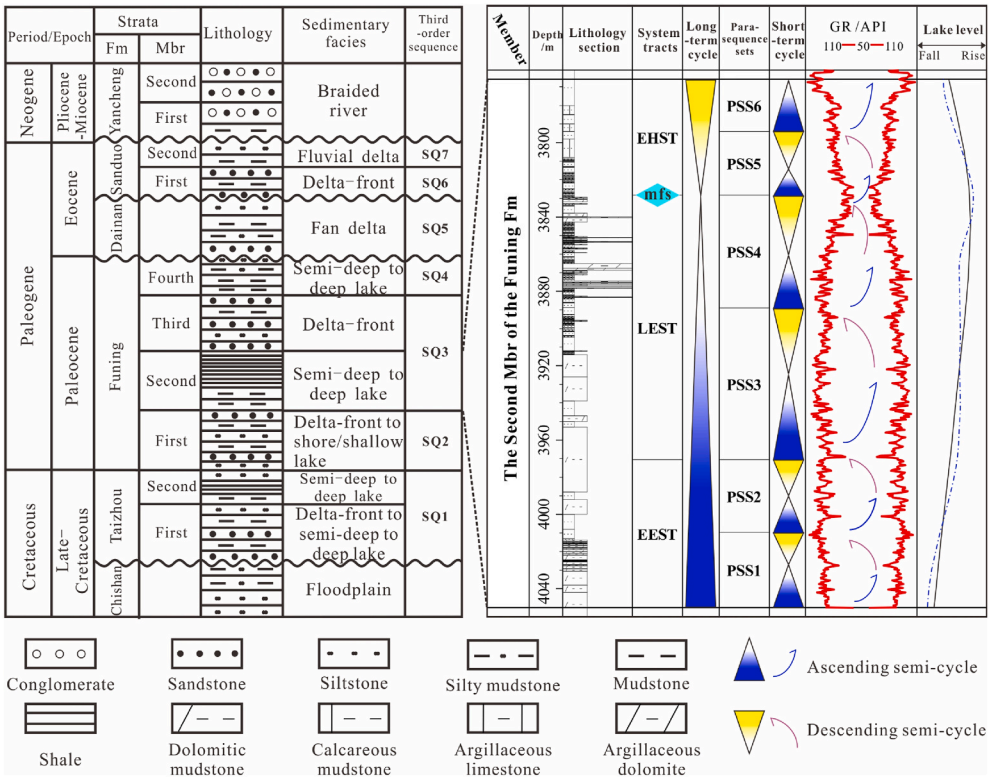

Fig. 2. Lithological column and sequence stratigraphic division from Late Cretaceous to Neogene in Haian Sag after Ran et al. (2012). The lithological column of the Second Mbr of the Funing Fm and corresponding sequence stratigraphic framework including three system tracts in third-order sequence and six parasequence sets (Guan, 2021). SQ = third-order sequence, EEST = early expanding system tract; LEST = late expanding system tract, EHST = early highland system tract; mfs = maximum flood surface, PSS = parasequence set.

hydrocarbon losses in previous studies, such as closed extraction technology (Wang, 2015), components simulation based on hydrocarbon generation kinetics (Xue et al., 2016), phase-state, and formation energy analysis (Chen et al., 2020; Zhang et al., 2014), hydrocarbon generation and expulsion mass balance method (Chen et al., 2018b), etc. Due to the strong heterogeneity of lacustrine shale, the generalization and applicability of these methods still need to be further verified.

The occurrence states are closely related to petroleum compositional characteristics (di Primio and Horsfield, 2006), impacting the production capacity and recovery of shale oil. Movable oil in shale is the petroleum resource that can be extracted under current economic and technical conditions (Zhang et al., 2012). Extractable oil is the light component of shale oil that can typically be extracted by stratum energy, and it is a part of movable oil (Zhu et al., 2021). Accurate evaluation of oil mobility is a prerequisite for the effective exploration and production of lacustrine shale oil. In this regard, the relationship between oil content parameters (S_1 and EOM) and organic matter abundance, such as Oil Saturation Index (OSI = S_1/TOC × 100) (Jarvie, 2012), the classification of TOC and S_1, TOC and chloroform bitumen "A" (Li et al., 2015; Lu et al., 2012), and free hydrocarbon difference (ΔS_1) (Li et al., 2016a), is frequently used to depict shale oil mobility. Some experimental methods, such as improved pyrolysis (Jiang et al., 2016a), sequential extraction (Zhang et al., 2020), saturation-centrifugal nuclear magnetic resonance (NMR) tests (Gong et al., 2020), two-dimension NMR tests (Li et al., 2020d), and so on, have been used to distinguish different petroleum groups and to determine movable oil in shales. In addition, Zhang et al. (2014) established a formation energy-driven production model to determine underground hydrocarbon compositions and production. From a microscopic standpoint, Wang et al. (2015) and Sui et al. (2020) investigated the phase-state characteristics of hydrocarbon fluids in a limited space using molecular dynamics simulation; and Li et al. (2017) developed a mathematical model to evaluate adsorbed oil amount, free oil amount, and their ratio using a hydrocarbon vapor adsorption test. However, these schemes evaluating shale oil mobility have their own application limitations to varying degrees. For example, lacustrine shales with high heterogeneity may have low S_1, low TOC, and high OSI, resulting in an error in assessing the movable oil in the shale; some experimental analyses, such as sequential extraction and NMR tests, are costly and time-consuming; a model driven by formation energy necessitates a large number of fundamental data, such as porosity, rock mechanical properties, oil saturation, gas-oil ratio (GOR), crude oil saturation pressure, etc., which is unsuitable for the majority of lacustrine shales at the early stages of exploration; and there is a gap between the simulation results and geological reality, because molecular dynamics simulation, which can only be applied to a limited pore size range and a single hydrocarbon component, can not accurately reflect the complex compositional characteristics of lacustrine shale oil currently. For the strongly heterogeneous lacustrine shale, it is urgent to establish a suitable, economic, and efficient method for evaluating oil content and mobility.

Lacustrine shales in eastern China are mostly from Cenozoic and Mesozoic, and present relatively low thermal maturity and relatively weak diagenesis evolution, resulting in a low GOR, high density of crude oil, and complicated spatial distribution of shale oil (Li et al., 2020a; Wang et al., 2019). Previous work paid more attention to shale oil content characterization (Jarvie, 2012; Li et al., 2015, 2018, 2020c; Lu et al., 2012; Jiang et al., 2016a). Although some research has discussed the oil content variation vertically based on measured samples or logging interception (Jarvie, 2012; T. Hu et al., 2018a; Li et al., 2016a; Liu et al., 2021), research on the spatial occurrence of shale oil is still scarce due to the strong heterogeneity of lacustrine shale and the lack of proper parameters representing the shale oil content.

The shale oil content of the Second Mbr of the Funing Fm (corresponding to E_1f^2 shale in Chinese stratigraphic notation) in Haian Sag, Subei Basin, is accurately characterized in the study based on petroleum compositional characteristics using a combination of light hydrocarbon restoration and chemical kinetics decomposition and reconstruction of hydrocarbon groups. As a result, the spatial distribution of shale oil in the Second Mbr of the Funing Fm is determined, and the controlling factors of oil content and mobility in the lacustrine shale are discussed.

This study presents a novel quantitative characterization of the diverse oil contents in lacustrine shales by recovering the loss of light hydrocarbons during different stages and decomposing-reconstructing pyrolysis hydrocarbons. It is significant to prioritize favorable shale oil exploration targets and to understand lacustrine shale oil accumulation and occurrence, which provides the effective parameters for calculating shale oil reserves.

2. Geological setting

Subei Basin, located in the east of China (Fig. 1a), has experienced multi-period tectonic movements since the Cretaceous, including regional depression in the late Cretaceous, fault depression in Paleogene, and overall subsidence depression in Neogene. Haian Sag, with an area of 3200 km^2, is located in the Subei Basin's southeast (Fig. 1b). The sag-controlling faults divide it into seven sub-sags and a high, including Sunjiawan Sub-sag, Fengbei Sub-sag, Xincao Sub-sag, Fu'an Sub-sag, Xinjie Sub-sag, Haibei Sub-sag, Qutang Sub-sag, and Haizhong High (Chen et al., 2009; Wang et al., 2012). The Qutang Sub-sag and the Haibei Sub-sag of the Haian Sag are two lacustrine rift basins governed by the Qutang and Beiling Faults, respectively (Fig. 1c) (Chen et al., 2012).

The sedimentary formations from Late Cretaceous to Tertiary include the Taizhou Formation in Cretaceous, the Funing Formation, the Dainan Formation and the Sanduo Formation in Paleogene, and the Yancheng Formation in Neogene (Shu et al., 2005) (Fig. 2). The Funing Formation is made up of lacustrine sediments with fluvial and transitional deposits and is divided into four members, from the first to the fourth member upward. The Second Mbr of the Funing Fm is mostly fine-grained sediment from semi-deep to deep lake facies, with mostly dark limy or dolomitic shale/mudstone lithologies. The buried depth of the Second Mbr of the Funing Fm is mostly from 2500 to 4500 m with a thickness of 150–400 m. The Second Mbr of the Funing Fm is the dominant source rock in the Haian Sag (Hu et al., 2018b).

The seismic reflection termination relationship demonstrates that a third-order sequence consists of the second member and third member of the Funing Formation (Ran et al., 2012). Furthermore, the high-frequency sequence stratigraphic framework of the Second Mbr of the Funing Fm is established by integrating wavelet transform technology with a natural gamma curve, and the Second Mbr of the Funing Fm consists of an early expanding system tract (EEST), a late expanding system tract (LEST), and an early highland system tract (EHST) in a third-order sequence, corresponding to six fourth-order sequences (Guan, 2021).

3. Sample and methods

3.1. Sample and experiment

All 24 samples were pulverized in tightly sealed apparatus cooled by online liquid nitrogen and then were applied to a Hawk Pyrolysis for pyrolysis analysis. Li et al. (2020c) describe the pyrolysis program in detail. FID signals were obtained, and parameters such as free hydrocarbon (S_1), thermal cracking hydrocarbon (S_2), peak temperature (Tmax), and hydrogen index (HI), among others, were quantified.

A Bruker D2 PHASER X-ray diffractometer was used to determine the mineral components. Powder shale samples (<300 mesh) were placed in the sample plate and then scanned from 4.5° to 50° with a step length of 0.02°. The identified mineral components' contents were calculated using the Rockquan+2012 software.

Thin sections were produced by being coated with epoxy resin and polished, and then were observed using a microscope under fluorescence light and reflected light.

Furthermore, existing data from the Zhejiang Oilfield was gathered to evaluate the spatial distribution and controlling factors of shale oil content in the Second Mbr of the Funing Fm, such as pyrolysis S_1 from geochemical logging and pyrolysis experiments, mineral components from X-ray diffractometer, and crude oil density.

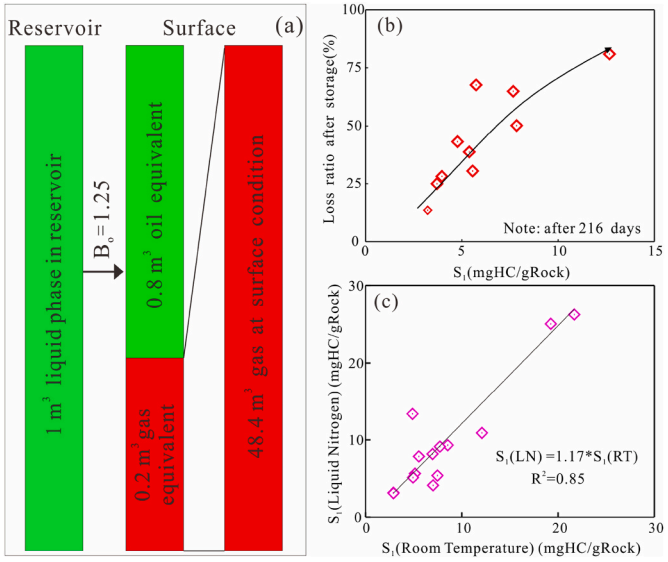

Fig. 3. Gaseous and light hydrocarbon loss during the different processes: (a) gaseous hydrocarbons loss caused by volumetric changes under different physical conditions during drilling and sample collection (Chen and Jiang, 2020); (b) correlation between S1 and light hydrocarbons loss ratio during sample storage (Qian et al., 2019); and (c) plot of S1 (RM) and S1 (LN) showing light hydrocarbons loss from sample pretreatment (Qian et al., 2019).

3.2. Shale oil content evaluation methods

3.2.1. Restoration of lost light hydrocarbon

There is a significant loss of gaseous and light hydrocarbons (S_{1L}) in shale samples from sample collection to testing, which mainly includes three stages: 1) When drilling and coring, the phase balance in the sample is broken due to changing temperature and pressure conditions from the reservoir to the ground, and the single-phase liquid hydrocarbon under the formation conditions transforms into two-phase gas and liquid. Because the pore space cannot accommodate the expanded gaseous hydrocarbons, the gaseous hydrocarbons quickly dissipate (Chen et al., 2020), resulting in S_{1LC} (Fig. 3a). 2) The sample is stored in the core library, and the light hydrocarbon components in the sample slowly dissipate due to a lack of packaging and sealing (Beti et al., 2020; Qian et al., 2019), which is S_{1LS} (Fig. 3b). And the longer the storage time, the greater the loss of light hydrocarbons. 3) Before testing, samples are pulverized at room temperature in the laboratory and the original storage conditions are destroyed. Some light hydrocarbon dissipates during this process (Qian et al., 2019), and this part is S_{1LP} (Fig. 3c).

Due to the lack of fresh coring samples of the Second Mbr of the Funing Fm in Haian Sag, the conditions for in-site testing are not available. To accurately evaluate the oil content of the Second Mbr of the Funing Fm, it is necessary to restore gaseous and light hydrocarbons.

When the shale formation is in the oil generation window or wet gas generation stage, the hydrocarbons in the reservoir are typically oils or condensates with some dissolved gaseous hydrocarbons (di Primio and Horsfield, 2006). Following the collection of the sample from the reservoir to the ground, changing temperature and pressure conditions result in the progressive exsolution of the gaseous hydrocarbon. The original pore space is unable to contain the expanded gaseous hydrocarbon, and gaseous hydrocarbon components escape from samples. These components of gaseous hydrocarbons are identical to the natural gas released after crude oil is collected on the ground from the reservoir. Chen and Jiang (2020) proposed a novel method for estimating gaseous

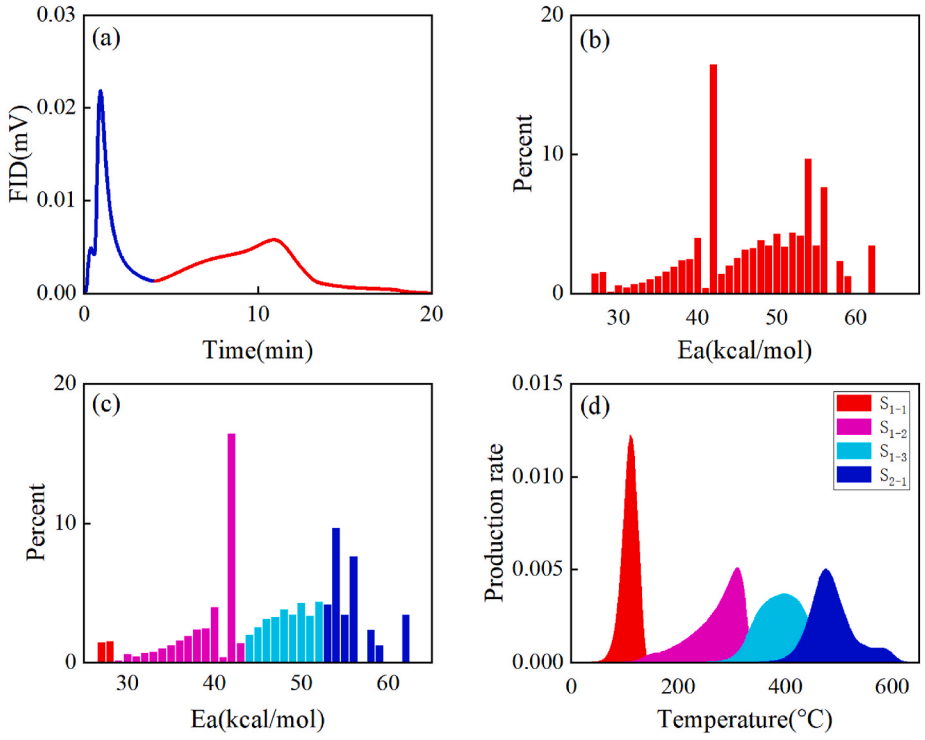

Fig. 4. Diagram showing decomposition and reconstruction of hydrocarbon groups by using FID programs: (a) FID signal from regular pyrolysis; (b) the Ea distribution derived from the FID signal based on chemical kinetics transformation; (c) the Ea distributions after splitting based on components properties; and (d) four petroleum groups determined by the corresponding Ea distributions.

hydrocarbon loss based on reservoir fluid phase behavior equations. The crude oil formation volume factor (B_o) and the pyrolysis data are used to calculate the gaseous hydrocarbon loss of the sample. By appropriating S_{1LC} as the natural gas released from crude oil as a result of phase behavior change, S_{1LC} can be determined by the oil mass difference between the reservoir condition and the surface condition.

According to mass balance, the mass of underground crude oil (m^R_{oil}) is equal to the mass of crude oil after degassing (m^S_{oil}) plus the mass of natural gas (m^S_{gas} or S_{1LC}) on the ground:

$$m^R_{oil} = m^S_{oil} + m^S_{gas} \tag{1}$$

In this study, sample pretreatment in cooled conditions by online liquid nitrogen causes little or no loss of light hydrocarbons. As a result, the weight of oil on the ground is equal to the sum of S_1 and S_{1LS}. S_{1LP} is a must-consideration for S_1 with sample pretreatment at room temperature. When B_o is the ratio of the volume of crude oil in the reservoir to the volume on the ground, formula (1) can be transformed into

$$m^R_{oil} = (S_1 + S_{1LS} + S_{1LP}) * B_o * \frac{\rho^R_{oil}}{\rho^S_{oil}} \tag{2}$$

where ρ^S_{oil} is the density of crude oil after degassing on the ground, and the density (20 °C) of the E_2f_1 shale crude oil produced in J204 and QX1 wells are 856.7 kg/m^3 and 868.4 kg/m^3, respectively. Therefore, the crude oil density of the shale oil in the Second Mbr of the Funing Fm is supposed to be 860 kg/m^3; ρ^R_{oil} is the crude oil density in the reservoir, which can be determined by the surface crude oil density and GOR:

$$\rho^R_{oil} = GOR * \frac{\rho^S_{gas}}{B_o} + \frac{\rho^S_{oil}}{B_o} \tag{3}$$

The amount of gaseous hydrocarbon loss during coring can be obtained:

$$m^S_{gas} = S_{1LC} = (S_1 + S_{1LS} + S_{1LP}) * \left(B_o * \frac{\rho^R_{oil}}{\rho^S_{oil}} - 1 \right) \tag{4}$$

S_{1LS} is affected by many factors, so it is difficult to determine the loss amount during the storage stage by exploring the influence of a single factor. In this regard, the loss of light hydrocarbons during storage can be calculated by comparing the S_1 differences of samples taken at the same location at different times. S_{1LS} can be calculated by comparing the difference between S_1 derived from geochemical logging and Rock-Eval in the study.

By comparing the difference in S_1 between samples pulverized at cooled conditions by online liquid nitrogen and at room temperature, S_{1LP} can be determined. It has been discovered that low-temperature experimental conditions can significantly reduce the light hydrocarbon loss caused by the pulverizing process. Pyrolysis analysis is an important aspect of geochemical logging that has been widely applied to core and cuttings samples in the field of well drilling to obtain geochemical parameters and evaluate the hydrocarbon generation potential of source rocks. Usually, core and cuttings samples are collected from underground and the Rock-Eval is performed simultaneously. Thus, the pyrolysis S_1 derived from geochemical logging only has gaseous and light hydrocarbon loss during the processes of drilling, coring, and sample pretreatment.

3.2.2. *Petroleum compositional grouping*

The rate constant for thermal evaporative kinetics depends on the reaction temperature, and the formulation of evaporative kinetics shows a similar form to that of chemical reaction (Penner, 1952). As a result, the thermal evaporative behavior can be described using a chemical reaction formulation. Li et al. (2018, 2020c) and Chen et al. (2018) considered petroleum thermal evaporation in an open pyrolysis system to be pseudo-thermal decomposition and proposed a mathematical method for separating different substances in shale. Here we use pseudo-chemical reaction kinetics to differentiate different petroleum

Table 1
Sample list and results of Rock-Eval in the Second Mbr of the Funing Fm.

No.	Well Name	Depth (m)	S_1 (mgHC/gRock)	S_2 (mgHC/gRock)	Tmax (°C)	TOC (wt.%)	HI (mgHC/gRock)	OI ($mgCO_2$/gRock)
1	J19	3808.24	1.03	7.59	445	3.08	246	13
2	J19	3813.70	0.46	4.32	446	2.26	191	14
3	J19	3818.55	1.59	7.09	446	2.93	242	11
4	J19	3823.49	1.46	12.87	447	3.41	377	14
5	J19	3825.05	2.25	23.79	446	5.40	440	7
6	J19	3841.45	1.60	2.90	431	2.45	118	21
7	J19	3848.30	0.24	1.50	437	0.91	164	69
8	J19	3853.00	0.63	2.84	439	1.70	167	38
9	J19	3857.71	3.38	11.24	444	3.97	282	8
10	J19	3878.25	0.30	1.65	438	1.16	142	46
11	J19	3886.00	0.65	2.42	439	1.53	158	29
12	J19	3888.00	1.01	3.07	443	1.46	210	35
13	J19	3890.90	0.98	2.46	433	1.42	172	33
14	J19	3895.00	2.87	6.76	437	2.43	278	12
15	J19	3902.36	1.47	2.78	445	1.22	227	27
16	J19	3908.40	1.26	3.99	440	1.67	239	23
17	J19	3911.65	1.12	3.69	439	1.65	223	24
18	J19	4015.05	1.94	3.33	437	1.76	189	18
19	J19	4021.05	1.69	2.54	437	1.47	173	22
20	J19	4028.50	4.18	7.84	435	2.86	274	19
21	J7	3559.15	0.05	0.32	429	0.65	48	85
22	J106	3558.60	0.21	1.94	443	1.17	165	28
23	J204	4283.75	0.04	0.11	446	0.74	15	42
24	G1	1323.71	0.07	3.28	436	1.55	211	39

Note: TOC = Total organic carbon; OI = Oxygen index.

substances with similar or identical physical and chemical properties. Let x represent the effective carbon in shale samples with a hydrocarbon generation capacity, and f(x) be a function of x to describe the kerogen conversion hydrocarbon generation reaction. The thermal degradation process of kerogen in source rock can be approximated as follows (Burnham and Braun, 1999):

$$\frac{dx}{dt} = \sum_{k=1}^{m} a_k k_k f(x_k) \tag{5}$$

where a_k is the relative contribution of the kth component, and k_k represents the reaction rate constant dependent on temperature that can be determined using the Arrhenius equation:

$$k_k = A^* exp\left(-\frac{E_k}{RT}\right) \tag{6}$$

A new formula to reflect the mixture of three types of thermal products during programmed pyrolysis is expressed as follows (Chen et al., 2018; Li et al., 2020c):

$$-\frac{d_x}{d_t} = \sum_{i=1}^{l} a_i k_i f(x_i) + \sum_{j=1}^{m} a_j k_j f(x_j) + \sum_{k=1}^{n} a_k k_k f(x_k) \tag{7}$$

where the first term on the right side is the thermal evaporative components; the second term is the thermal decomposition equivalent part of pseudo-kerogen, such as heavy oil or asphalt; and the third term is the thermal degradation product of kerogen. In the equation, l, m, and n represent the number of (pseudo) activation energies for free hydrocarbons, heavy oil or asphalt, and kerogen, respectively.

The activation energy distribution of the three different components in different thermal reaction processes can be calculated using the same frequency factor (A), as can the mixed activation energy distribution of the entire pyrolysis process. A more generalized expression is shown as follows (Burnham and Braun, 1999; Chen et al., 2017a, 2017b):

$$x = \int_0^{\infty} exp\left[-A\int_0^{t} k(T)dt\right] D(E)dE \tag{8}$$

where D(E) is the activation energy density function and $\int_0^{\infty} D(E)dE = 1$.

The non-dimensional discrete activation energy distribution model is used to describe the changing products in different processes.

In this study, Kinetics 2015 software was used to realize the decomposition and reconstruction of hydrocarbon components. The specific operation process is as follows:

1) Use the module of "analysis" in Kinetics2015 software to convert the original pyrolysis FID curve into the activation energy distributions of thermal evaporative hydrocarbon products and thermal degradation hydrocarbon products (heavy hydrocarbons or asphalt, and kerogen) (Fig. 4a and b);
2) According to the relative contribution of thermal evaporative products (S_1) and thermal degradation products (S_2), the activation energies of thermal evaporative hydrocarbon products and thermally degradation products (heavy hydrocarbons or asphalt, and kerogen) are jointed to establish the entire mixed activation energy distribution (Fig. 4b);
3) The activation energy distribution of samples can be divided into four parts. Each part is an assembly of components with similar physical and chemical properties, but the physical and chemical properties of each assembly are very different. The resulting activation energy distributions include a) the first with the lowest Ea of 25–28 kcal/mol corresponding to the low-molecular-weight oils; b) the second with a middle Ea of 29–43 kcal/mol that is mid-to high-molecular-weight oils; c) the third with Ea of 44–52 kcal/mol that is mostly heavy oil or bitumen; d) the last one with the highest Ea of 53–67 kcal/mol corresponding to kerogen (Fig. 4c). The Ea ranges of different groups are similar to those of the Qiangjiang Formation in Jianghan Basin (Li et al., 2020c);
4) In Kinetics2015 software, use the "Apply" module to calculate the relative yields of different groups, assign the hydrocarbon generation potential ($S_1 + S_2$) based on the relative contribution of different groups, and quantify different groups (Fig. 4d).

4. Results

4.1. Geochemical and petrological characteristics

4.1.1. Bulk geochemical characteristics

The geochemical parameters from Rock-Eval are listed in Table 1.

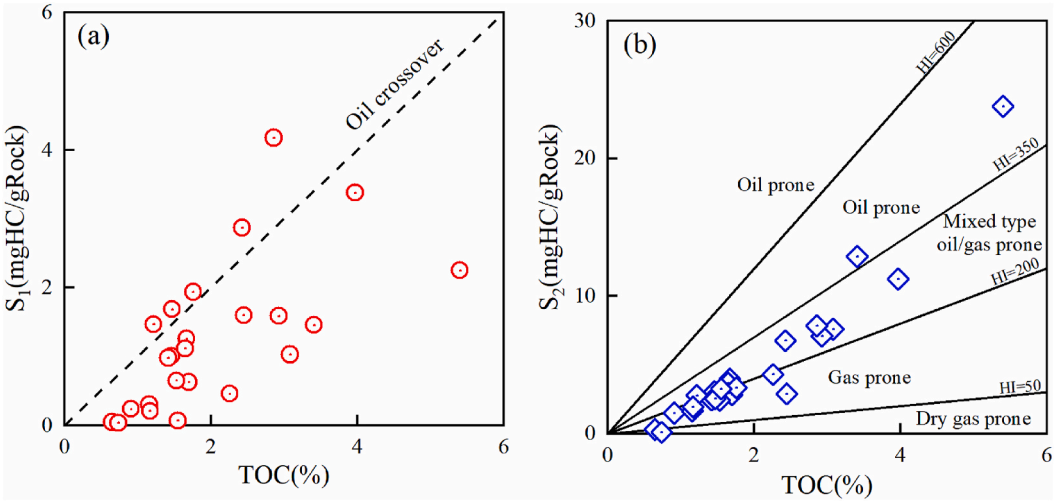

Fig. 5. Geochemical characteristics of the Second Mbr of the Funing Fm: (a) plot of TOC vs S_1 shows oil crossover for some shale samples and confirms good shale oil potential for the Second Mbr of the Funing Fm; and (b) plot of TOC vs S_2 demonstrates various organic matter types in the Second Mbr of the Funing Fm.

Table 2
Mineral components of the Second Mbr of the Funing Fm.

Well Name	Depth (m)	Mineral components (wt, %)							
		Clay	Quartz	Feldspar	Calcite	Dolomite	Siderite	Pyrite	Analcime
G1	1323.71	42.8	19.7	12.8	12.4	9.7	0.5	0.5	–
J19	3825.05	30.4	31.2	4.7	27.8	–	–	4.2	–
J19	3848.30	42.7	18.3	5.0	20.8	12.2	–	–	–
J19	3865.65	33.1	24.0	4.9	1.7	26.6	–	–	6.6
J19	3867.23	43.3	28.8	3.2	23.3	–	–	–	–
J19	3886.00	36.3	18.3	5.6	10.6	16.3	–	3.0	9.9
J19	3895.00	30.8	23.4	9.5	16.1	17.2	–	3.0	–
J19	3902.36	17.7	22.4	11.6	9.7	31.9	–	6.8	–
J19	3905.20	30.6	14.2	4.2	10.2	12.1	26.3	2.5	–
J19	3914.00	39.7	24.1	9.2	14.1	9.5	–	3.4	–
J19	3942.00	27.1	16.4	13.2	16.6	20.8	–	2.8	–
J19	3956.00	31.3	22.2	12.1	27.4	–	–	–	4.3
J19	3977.00	22.0	16.3	9.3	21.0	24.6	–	2.5	3.3
J19	3986.00	29.9	15.1	7.0	11.6	21.7	–	2.8	9.2
J19	4001.00	29.6	17.5	9.8	23.8	14.9	–	1.5	–
J19	4013.00	27.1	18.1	14.2	15.2	19.0	–	3.8	–
J19	4015.05	22.4	18.7	10.7	14.1	27.1	–	6.9	–
J19	4021.05	13.3	12.5	8.9	13.4	45.5	–	–	–
J19	4028.50	19.3	12.9	14.2	7.7	38.6	–	–	–
J19	4036.00	19.7	20.1	14.5	14.0	26.3	–	4.4	–
J19	4048.00	22.0	18.2	11.6	13.3	29.1	1.1	3.9	–
J19	4052.00	24.7	17.0	7.6	20.3	26.7	–	3.7	–
J204	4022.68	41.0	20.2	3.2	15.5	14.7	4.5	0.9	–
J204	4024.41	49.4	28.1	10.9	10.1	–	–	–	–
J204	4026.53	35.7	16.3	2.6	14.3	–	28.7	1.9	–
J204	4141.18	43.2	20.2	6.5	17.4	9.0	–	3.7	–
J204	4146.21	39.6	20.6	7.2	13.5	13.6	–	4.7	–
J204	4283.75	44.9	27.3	10.7	11.0	6.1	–	–	–
J204	4286.59	36.8	37.9	8.5	10.1	5.3	–	–	–

The Second Mbr of the Funing Fm shows medium to high organic abundance with TOC ranging from 0.65 wt% to 5.40 wt%, and the samples with TOC exceeding 1% are more than half. S_1 values vary from 0.04 to 4.18 mgHC/gRock, with an average of 1.27 mgHC/gRock. S_1 values rise as TOC rises, and some samples exhibit oil crossover (Fig. 5a). The S_2 values range from 0.11 to 23.79 mgHC/gRock, with a mean of 5.01 mgHC/gRock. A diverse TOC-S_2 zone demonstrates that various organic matter types, ranging from gas-prone to oil-prone, exist in the Second Mbr of the Funing Fm (Fig. 5b). Tmax values range from 429 °C to 447 °C, and Ro (vitrinite reflectance) values vary from 0.7% to 1.5% (Guan, 2021), indicating a wide range of thermal maturity.

4.1.2. Petrological characteristics

The primary minerals in the Second Mbr of the Funing Fm include clay, quartz, feldspar, calcite, dolomite, and siderite. Clay mineral content varies from 13.3% to 49.4% with an average of 31.9%; quartz content is from 12.5% to 37.9% with an average of 20.7%; feldspar content has a range of 2.6%–14.5% and an average of 8.7%; calcite content ranges from 1.7% to 27.8% with an average of 15.1%; dolomite content varies from 5.3% to 45.5% with an average of 19.9%. Siderite content is relatively low, except for two samples that exceed 26% (Table 2). The Second Mbr of the Funing Fm shows relatively even primary mineral content and mainly belongs to clay-rich mixed shale and carbonate-rich mixed shale (Fig. 6).

The sedimentary structure is an important indicator that can reflect

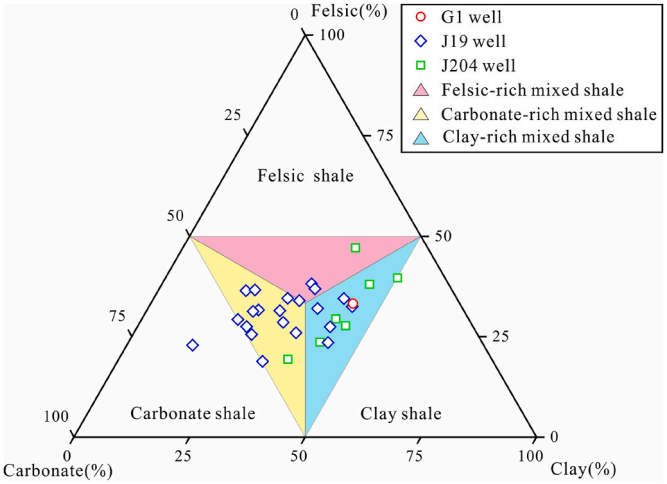

Fig. 6. Lithofacies determined by the mineral compositions showing predominant clay-rich mixed shale and carbonate-rich mixed shale in the Second Mbr of the Funing Fm.

paleoclimate and paleoenvironment at the stage of shale deposition. The sedimentary structure of shale can be classified as laminae (fractions of millimeters to millimeters in thickness), bed (millimeters to tens of centimeters in thickness), and massive structure (more than tens of centimeters in thickness) (Lazar et al., 2015). Massive and lamellar structures are more common than bedded structures in the Second Mbr of the Funing Fm. The massive structure is most common in pure mudstone with a high clay content (Fig. 7a and b), whereas the lamellar structure in the Second Mbr of the Funing Fm consists primarily of organic matter laminae, carbonate laminae, and clay laminae (Fig. 7c and d).

4.2. Estimation of oil content

4.2.1. Estimation of gaseous and light hydrocarbon loss

(1) Loss of gaseous hydrocarbon at the process of drilling and coring

There is a lack of measured GOR data for the Second Mbr of the Funing Fm in Haian Sag. Based on the correlation between GOR and the depth of the Second Mbr of the Funing Fm in the adjacent Qintong Sag, GOR is determined to be 9–51 m^3/m^3 with a depth range of approximately 2000–4300 m (Guan, 2021). GOR and Bo usually have a good correlation. According to the relationship between GOR and B_o of the Upper Devonian Duvernay Formation shale oil in the Western Canada Basin (Chen et al., 2019), the GOR of 9–51 m^3/m^3 corresponds to a B_o of about 1.04–1.20. According to the relative contribution of C_1–C_5 from gas logging in the Second Mbr of the Funing Fm, the density of gaseous

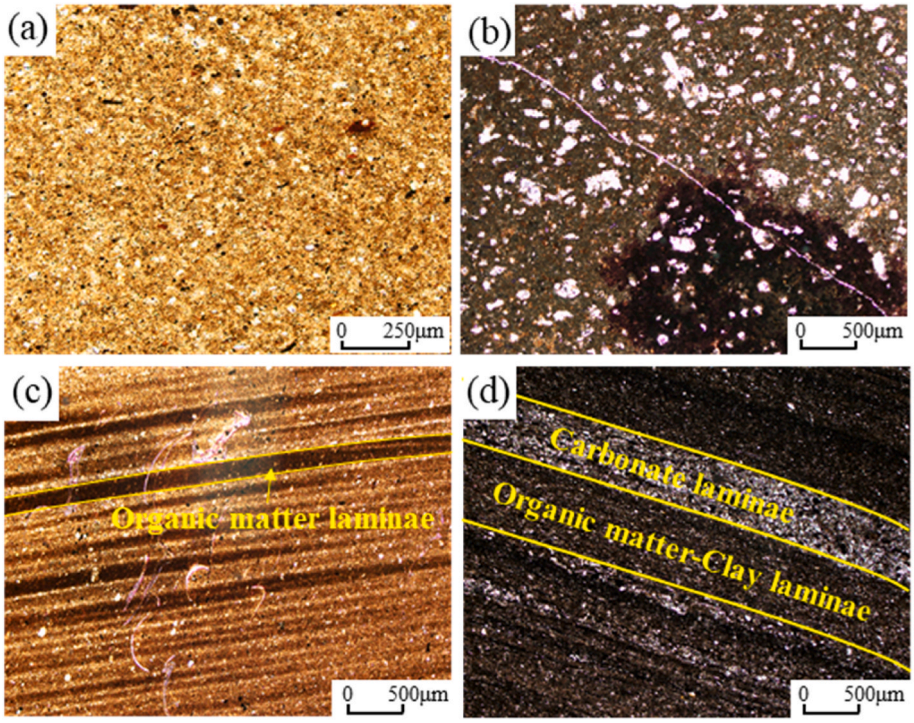

Fig. 7. Thin-section photographs showing sedimentary structure characteristics in the Second Mbr of the Funing Fm: (a) Ji19 well, 3809.40 m, massive mudstone; (b) Ji19 well, 3840.25 m, massive silty dolomite mudstone; (c) Ji19 well, 3923.5 m, clay-organic laminae in lime mudstone; and (d) Ji19 well, 3850 m, carbonate-organic matter and clay laminae in the calcite-bearing dolomitic mudstone.

Table 3
Hydrocarbon loss of the Second Mbr of the Funing Fm during sample storage.

No.	Well name	Depth/ m	S_1 from logging well/ mgHC·gRock^{-1}	S_1 in the study/ mgHC·gRock^{-1}	S_{1LS}/ mgHC·gRock^{-1}	Loss rate/ %
1	J19	3808.24	2.39	1.03	1.36	57
2	J19	3813.70	1.18	0.46	0.72	61
7	J19	3848.30	0.36	0.24	0.12	33
17	J19	3911.65	1.94	1.12	0.82	42

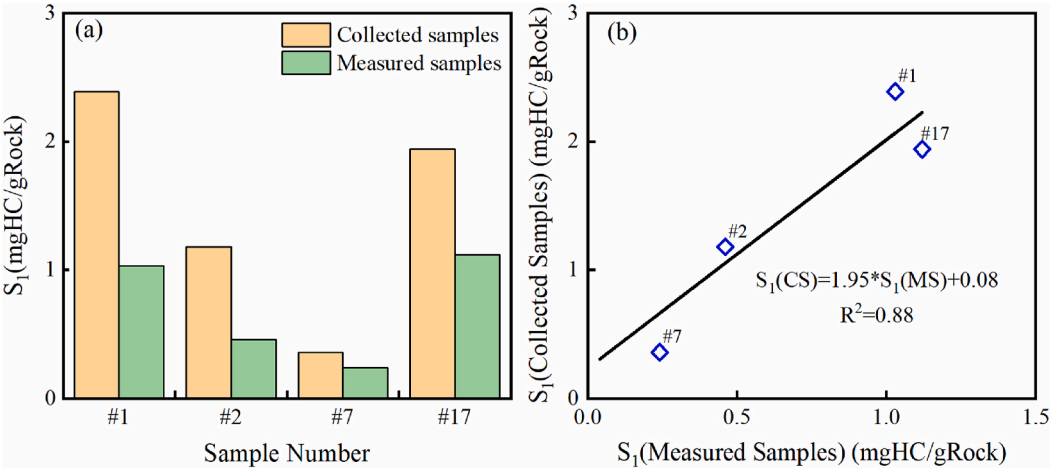

Fig. 8. Pyrolysis S_1 differences between after drilling and in the study showing hydrocarbon loss of the Second Mbr of the Funing Fm during sample storage: (a) histogram; and (b) plot of the collected existed data vs measured data in the study.

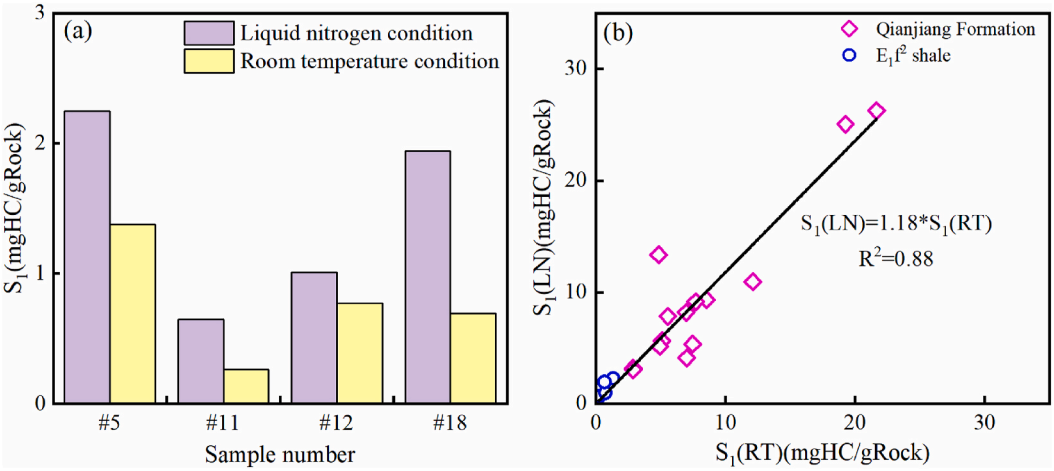

Fig. 9. Pyrolysis S_1 from crushing sample in liquid nitrogen condition and at room temperature condition showing hydrocarbon loss during sample storage for the Second Mbr of the Funing Fm: (a) histogram and (b) plot of pyrolysis S_1 from liquid nitrogen condition and room temperature conditions.

hydrocarbons on the surface is about 1.05 kg/m^3. Thus, S_{1LC} in the Second Mbr of the Funing Fm accounts for about 1%–6% of S_1 via Eq. (3) and Eq. (4) in the study, and S_{1LC} increases as the burial depth increases. The low GOR in the Second Mbr of the Funing Fm is caused by the high crude oil density, low gaseous hydrocarbon content from gas logging data, and a high percentage of C_2–C_5 content, which accounts for approximately 70%. As a result, the amount of gaseous hydrocarbons lost during the drilling and coring processes is minimal.

(2) Loss of light hydrocarbon at the process of sample preservation

The S_1 differences between geochemical logging and measured samples in this study are obtained to determine the loss amounts of shale oil during sample preservation. The result shows that the amount of light hydrocarbons lost is 0.12–1.36 mgHC/gRock and the loss rate is 33%–61%. (Table 3 and Fig. 8). The greater the original S_1 in the sample, the greater the amount of light hydrocarbon lost. According to the comparison results, using S_{1LS} and the S_1 tested in this study to establish a recovery model for S_{1LS}:

$$S_{1LS} = 0.95 \times S_1 + 0.08 \quad (9)$$

(3) Loss of light hydrocarbon at the process of sample pretreatment

The loss amount of light hydrocarbons in the Second Mbr of the Funing Fm caused by sample pulverization at room temperature is be-

Table 4
Hydrocarbon loss of the Second Mbr of the Funing Fm during sample preparation.

No.	Well Name	Depth/m	Room temperature condition		Liquid nitrogen cooling condition		S_{1LP}/ mgHC·gRock^{-1}
			S_1/ mgHC·gRock^{-1}	S_2/ mgHC·gRock^{-1}	S_1/ mgHC·gRock^{-1}	S_2/ mgHC·gRock^{-1}	
5	J19	3825.05	1.38	21.93	2.25	23.79	0.87
11	J19	3886.00	0.26	2.34	0.65	2.42	0.39
12	J19	3888.00	0.77	3.03	1.01	3.07	0.24
18	J19	4015.05	0.70	3.00	1.94	3.33	1.24

Table 5
Petroleum composition grouping results from light hydrocarbon restoration and the chemical kinetic decomposition.

No.	A (s^{-1})	Pyrolysis parameters (mgHC/gRock)		Computed groups (mgHC/gRock)					Various shale oil content/ (mgHC/gRock)		
		S_1	S_2	S_{1L}	S_{1-1}	S_{1-2}	S_{1-3}	S_{2-1}	S_T	S_M	S_P
1	1.3×10^{14}	1.03	7.59	1.22	0.24	0.87	1.18	6.34	3.50	2.33	1.46
2	6.0×10^{14}	0.46	4.32	0.54	0.13	0.39	0.57	3.69	1.64	1.06	0.68
3	1.3×10^{14}	1.59	7.09	1.88	0.25	1.42	1.09	5.92	4.64	3.55	2.13
4	1.3×10^{14}	1.46	12.87	1.72	0.23	1.28	0.68	12.15	3.91	3.23	1.95
5	1.3×10^{14}	2.25	23.79	2.66	0.27	1.98	0.24	23.55	5.15	4.91	2.93
6	1.3×10^{14}	1.60	2.90	1.89	0.13	1.58	1.35	1.43	4.96	3.61	2.02
7	1.3×10^{14}	0.24	1.50	0.28	0.06	0.20	0.49	0.99	1.04	0.54	0.35
8	1.3×10^{14}	0.63	2.84	0.74	0.10	0.59	0.98	1.80	2.41	1.43	0.84
9	1.3×10^{14}	3.38	11.24	3.99	0.22	3.34	1.13	9.94	8.68	7.55	4.22
10	1.3×10^{14}	0.30	1.65	0.35	0.03	0.29	0.57	1.06	1.24	0.68	0.39
11	1.3×10^{14}	0.65	2.42	0.77	0.05	0.65	0.77	1.60	2.24	1.47	0.82
12	1.3×10^{14}	1.01	3.07	1.19	0.06	1.02	0.69	2.32	2.96	2.27	1.25
13	1.3×10^{14}	0.98	2.46	1.16	0.11	0.94	1.03	1.37	3.23	2.20	1.27
14	1.3×10^{14}	2.87	6.76	3.39	0.26	2.80	2.01	4.56	8.46	6.46	3.65
15	7.0×10^{14}	1.47	2.78	1.74	0.09	1.50	0.67	1.98	4.00	3.33	1.83
16	1.3×10^{14}	1.26	3.99	1.49	0.13	1.20	1.23	2.68	4.06	2.83	1.62
17	1.3×10^{14}	1.12	3.69	1.33	0.09	1.12	1.23	2.37	3.76	2.54	1.42
18	1.3×10^{14}	1.94	3.33	2.30	0.14	1.91	1.02	2.20	5.37	4.35	2.44
19	1.3×10^{14}	1.69	2.54	2.00	0.07	1.72	0.81	1.63	4.60	3.79	2.08
20	1.3×10^{14}	4.18	7.84	4.96	0.16	4.24	1.41	6.20	10.77	9.36	5.12
21	1.3×10^{14}	0.05	0.32	0.06	0.00	0.05	0.10	0.22	0.21	0.11	0.06
22	1.3×10^{14}	0.21	1.94	0.25	0.01	0.21	0.36	1.56	0.83	0.47	0.26
23	1.3×10^{14}	0.04	0.11	0.05	0.00	0.04	0.02	0.09	0.11	0.09	0.05
24	1.3×10^{14}	0.07	3.28	0.08	0.02	0.06	0.78	2.49	0.94	0.16	0.10

tween 0.24 and 1.24 mgHC/gRock (Fig. 9 and Table 4). Qian et al. (2019) found that the loss amount of light hydrocarbon is about 17% of S_1 at room temperature for Qianjiang Formation in Qianjiang Sag, Jianghan Basin. By integrating the pyrolysis results at different preparation conditions from Qianjiang Formation with that from the Second Mbr of the Funing Fm, S_{1LP} is about 18% of S_1 with sample pretreatment in room temperature (Fig. 9b):

$$S_{1LP} = 0.18 \times S_1(\mathrm{RT}) \quad (10)$$

4.2.2. Compositional grouping

(1) Activation energy characteristics

By fixing frequency factor A, pyrolysis programs of the 24 shale samples (Fig. S1) were converted into activation energy domains and the resulting Ea distributions were obtained (Fig. S2). Most samples have two distinct clusters, one with an Ea < 43 kcal/mol and the other with an Ea > 43 kcal/mol, corresponding to thermal evaporative and thermal degradation products, respectively. The S_1 curves and resulting Ea distributions are primarily derived from the thermal evaporation of low- and mid-molecular-weight petroleum compositions in samples. While the S_2 curves and the corresponding Ea distributions come from thermal evaporation and thermal decomposition of large-molecular-weight petroleum and kerogen. The Ea distributions from S_1 curves present unimodal or bimodal distributions, representing two major petroleum groups overall, including the one with an Ea of 25–28 kcal/mol and the other with an Ea of 29–43 kcal/mol. The Ea distributions derived from S_2 curves show unimodal or bimodal distributions, representing high-molecular-weight petroleum and kerogen that correspond to the Ea of 44–52 kcal/mol and 53–67 kcal/mol, respectively.

(2) Compositional characteristics

According to the Ea distribution mode of partition results, the Ea distributions of different sub-groups of the shale samples can be transformed into sub-group yields by using the fixing frequency factor A (Table 5). By reassembling the Ea distributions of these shale samples, the four sub-groups dependent on temperature space are reconstructed (Fig. 10), and each of them represents a group with close or similar physical and chemical properties. The first group in Fig. 10 represents the low-molecular-weight oils in samples and can be denoted by S_{1-1}; the second group in Fig. 10 is mid-to high-molecular-weight oils in samples and can be denoted as S_{1-2}; the third group in Fig. 10 denotes mostly heavy oil or bitumen in samples and can be identified as S_{1-3}; the last group in Fig. 10 is kerogen in samples and can be called S_{2-1}.

5. Discussion

5.1. Shale oil content evaluation model

Jiang et al. (2016a) demonstrated a range of nC_{10}–nC_{33} in the total hydrocarbon chromatogram of the lacustrine shale oil from the lower part of the third Mbr of the Shahejie Fm in Jiyang Depression and suggested low-molecular-weight hydrocarbons with the alkane maxima at nC_{16} and mid-to high-molecular-weight hydrocarbons with the alkane maxima at nC_{19}–nC_{25}. Given the similar sedimentary conditions, close hydrocarbon generation potential, and thermal maturity of the lower third Mbr of the Shahejie Fm and the second Mbr of the Funing Fm, petroleum compositions from the second Mbr of the Funing Fm may be comparable to those of the lower third Mbr of the Shahejie Fm. The petroleum content in the Second Mbr of the Funing Fm was demonstrated by S_{1-1}, S_{1-2}, and S_{1-3}, respectively. S_{1-1} is a low-molecular-weight hydrocarbon with a high concentration of nC_{20}^- alkanes; S_{1-2} is a mid-to high-molecular-weight hydrocarbon with predominant nC_{20}–nC_{30} alkanes; S_{1-3} is high-molecular-weight heavy oil in which nC_{30}^+ alkanes predominate.

Shale oil content and mobility can be evaluated according to various petroleum compositional characteristics. Total oil content (S_T) is the sum of all hydrocarbon components in the samples, including S_{1L}, S_{1-1}, S_{1-2}, and S_{1-3}. Movable oil content (S_M) is the sum of S_{1L}, S_{1-1}, and S_{1-2}, which represent the hydrocarbon component content of the samples other than adsorbed hydrocarbons. The producible oil content (S_P) is S_{1L} plus S_{1-1}, which denotes a gas and a light hydrocarbon with a low boiling temperature and viscosity. The oil content in sorption (S_S) is S_{1-3}, corresponding to bitumen and heavy hydrocarbons. The good correlations between pyrolysis S_1 and various oil contents, including S_T, S_M, and S_P

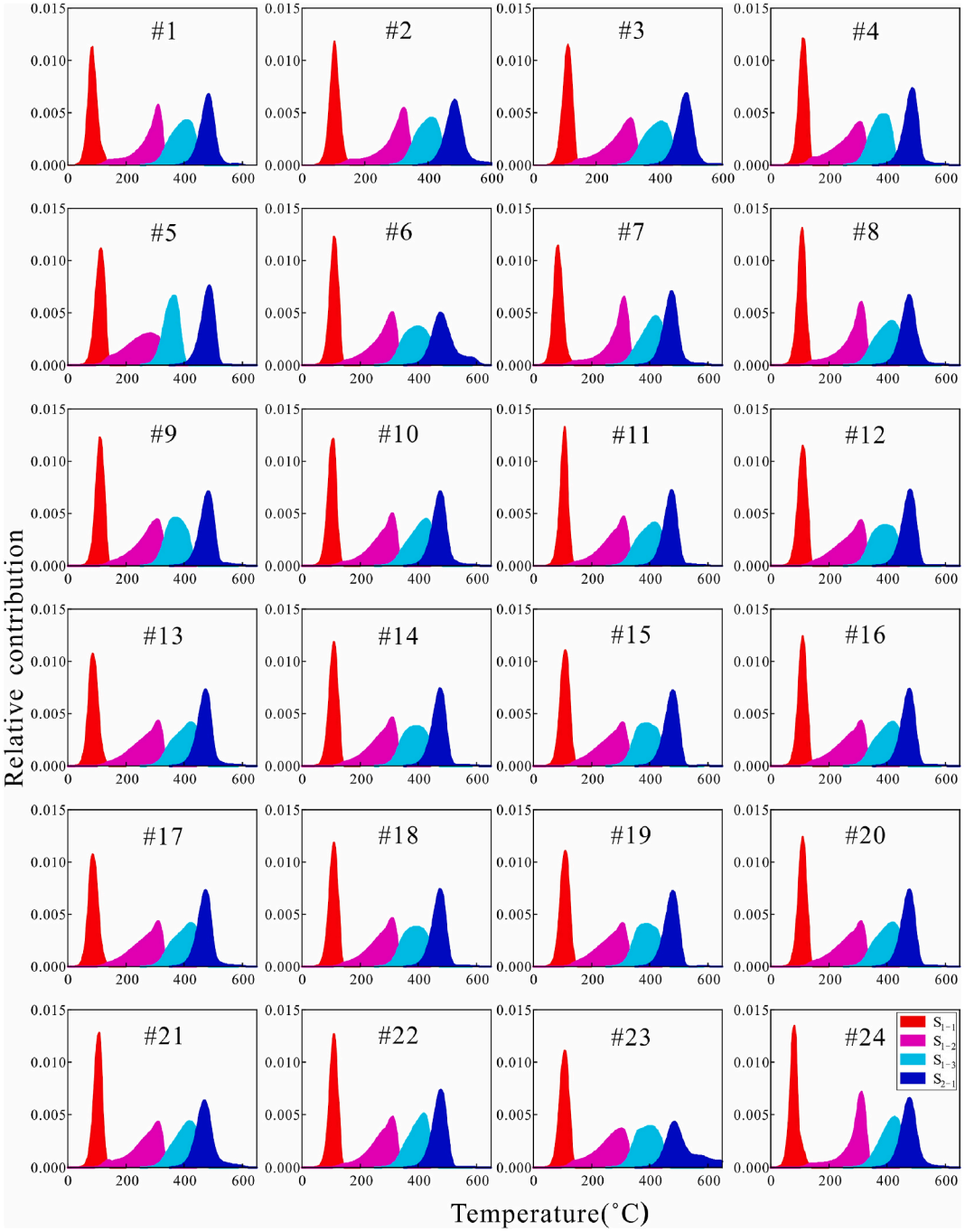

Fig. 10. Four petroleum compositional grouping constructed from FID pyrograms for the Second Mbr of the Funing Fm based on different physical/chemical properties: $S_{1\text{-}1}$ is low-molecular-weight oils; $S_{1\text{-}2}$ is mid-to high-molecular-weight oils; $S_{1\text{-}3}$ is mostly heavy oil or bitumen; and $S_{2\text{-}1}$ is kerogen.

(Fig. 11a–c), demonstrate that it may be feasible to evaluate various shale oil contents by using pyrolysis S_1 unavailable for decomposition and reconstruction of petroleum groups. Furthermore, the relationship between oil content in sorption and TOC is complicated. There is a positive correlation when TOC is less than 2%. However, when TOC exceeds 2%, the relationship between TOC and oil content in sorption is ambiguous (Fig. 11d), which could be due to the diversity of organic matter types and thermal maturity in different shale samples.

5.2. Spatial variations of shale oil content

The neural network model can integrate logging responses with the corresponding measured value and then quickly establish the nonlinear relationship between logging curves and measured data without considering their internal relationship. The Multilayer Perceptron (MLP) is a forward-structured artificial neural network that maps a group of input vectors to a group of output vectors and quickly establishes a nonlinear functional relationship between the input layer and the output layer via at least one hidden layer (Fig. S3). Therefore, MLP in Statistical Product and Service Solutions software is utilized to carry out logging prediction for shale oil content in the Second Mbr of the Funing Fm.

By integrating the S_T and the corresponding logging responses from a series of logging curves, including natural gamma (GR), spontaneous potential (SP), elemental capture spectroscopy (K, TH, and U), neutron (CNL), density (DEN), acoustic (AC), and resistivity (Rt), the evaluation model of shale oil content was established. By combining the logging

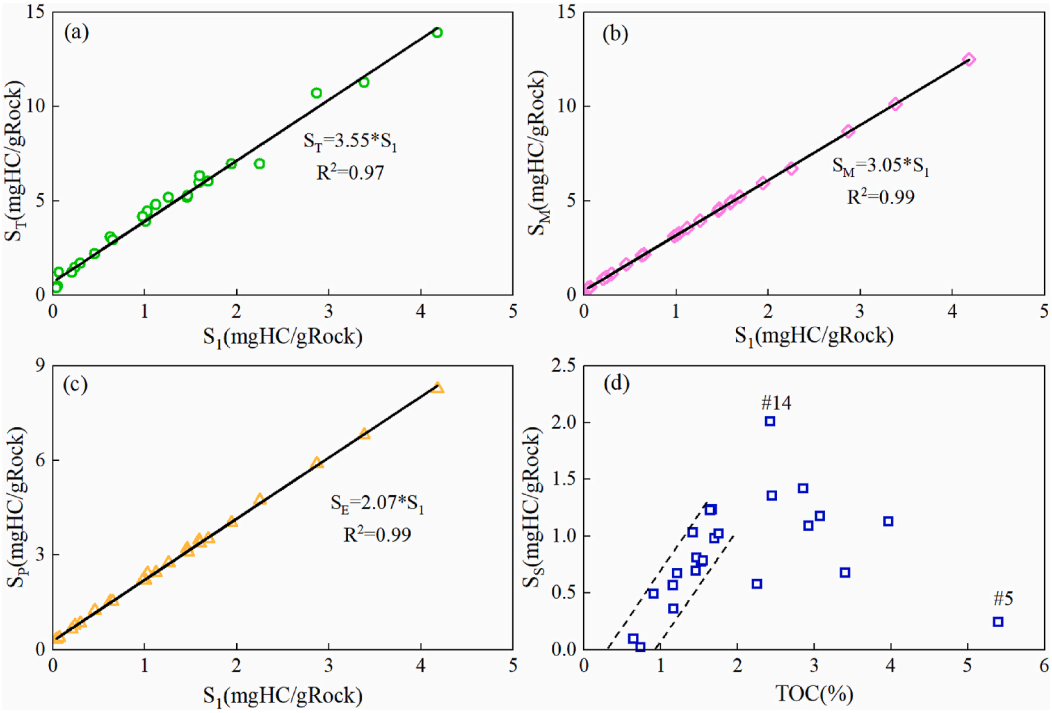

Fig. 11. The evaluation model for shale oil content of the Second Mbr of the Funing Fm derived from gaseous and light hydrocarbon restoration and reconstruction of petroleum composition groups: Plots of (a) S_1 and S_T, (b) S_1 vs S_M, and (c) S_1 vs S_E shows good correlation between S_1 and various oil contents (d) Plot of TOC vs S_S indicates a positive correlation appears when TOC is less than 2% and an ambiguous relationship between TOC and oil content in sorption when TOC exceeds 2%.

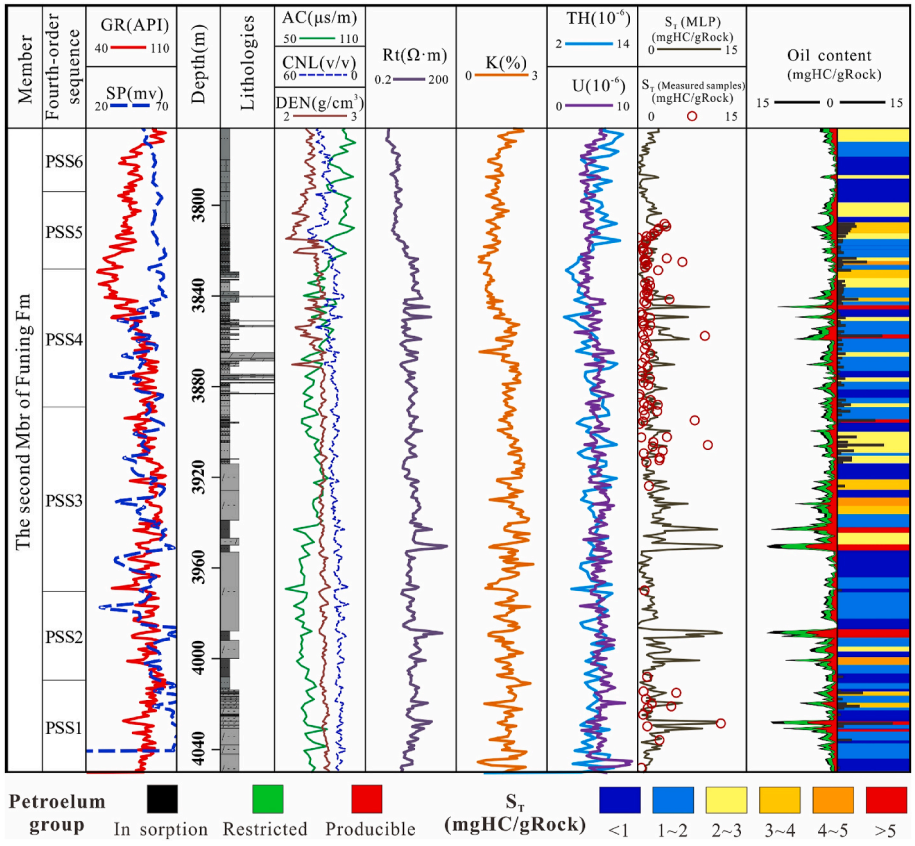

Fig. 12. The vertical variation of shale oil content for the Second Mbr of the Funing Fm in Ji19 was well determined by MLP logging prediction showing that multi-layers with high oil content mostly appear in PSS3, PSS4, and PSS5.

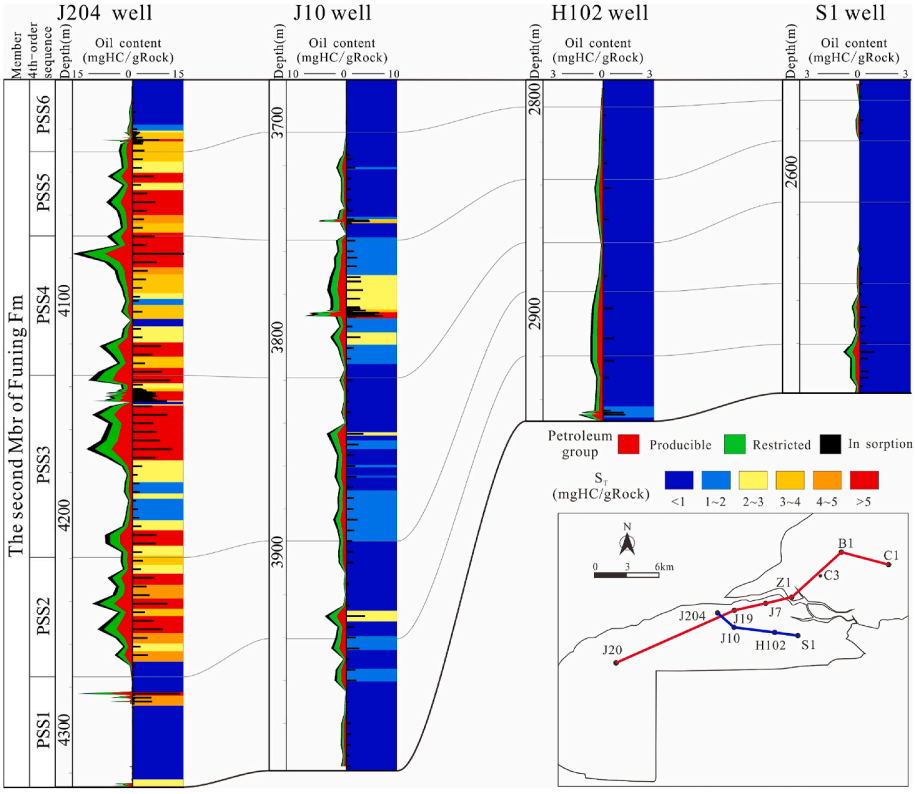

Fig. 13. The vertical variation of the shale oil content for Second Mbr of the Funing Fm in Haian Sag from northwest to southeast showing that J204 well in deep sag zone develops multi-layers with high oil content, some intervals in J10 wells have high oil content, and H102 and S1 wells in the slope area has a lowest oil content.

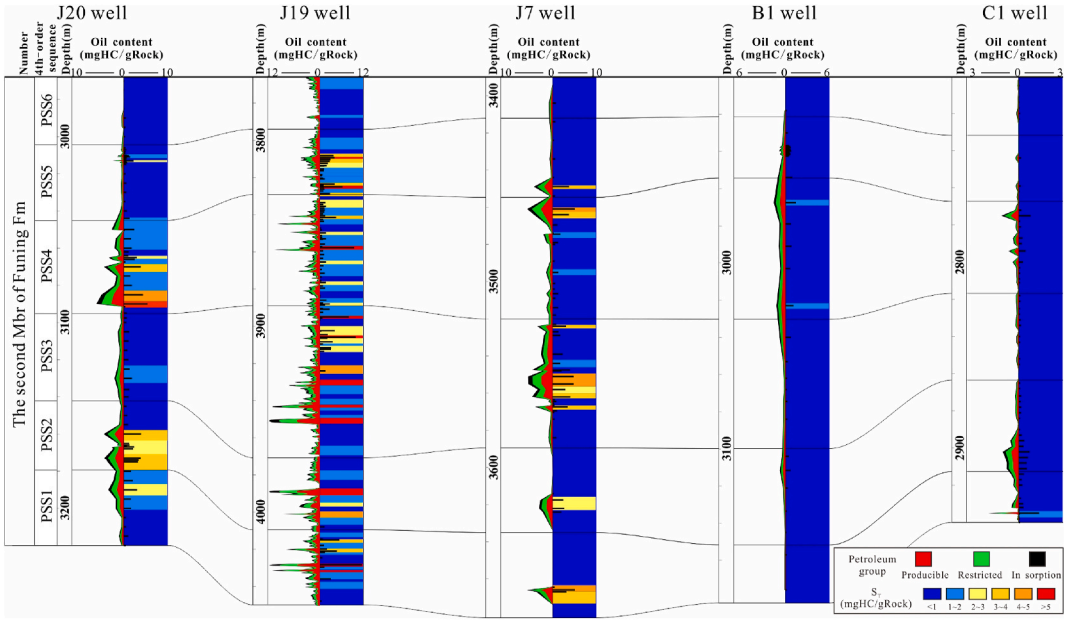

Fig. 14. The vertical variation of shale oil content for Second Mbr of the Funing Fm in Haian Sag from southwest to northeast showing that J19 well in deep sag zone develops multi-layers with high oil content, some intervals in J7 and J20 wells have high oil content, and B1 and C1 wells in Haibei Sub-sag have lowest oil content.

prediction model with logging responses, shale oil content can be predicted for the layer with no measured shale oil content. The S_T determined by the measured data is consistent with the logging prediction (Fig. S4), indicating that it is feasible to carry out the prediction of shale oil content in the Second Mbr of the Funing Fm using an MLP neural network. Furthermore, S_M and S_P can be calculated using a predicting S_T and a shale oil content evaluation model.

The vertical continuous distribution characteristics of shale oil in the J19 well were determined by combining S_T from measured data and logging prediction (Fig. 12). There are multi-layers with high S_T in the J19 well, mainly developing in the vicinity of the maximum flooding surface in third-order sequence and the ascending semi-cycle of the PSS3. This work lays the foundation for spatial heterogeneous distribution evaluation of the shale oil content in the Second Mbr of the

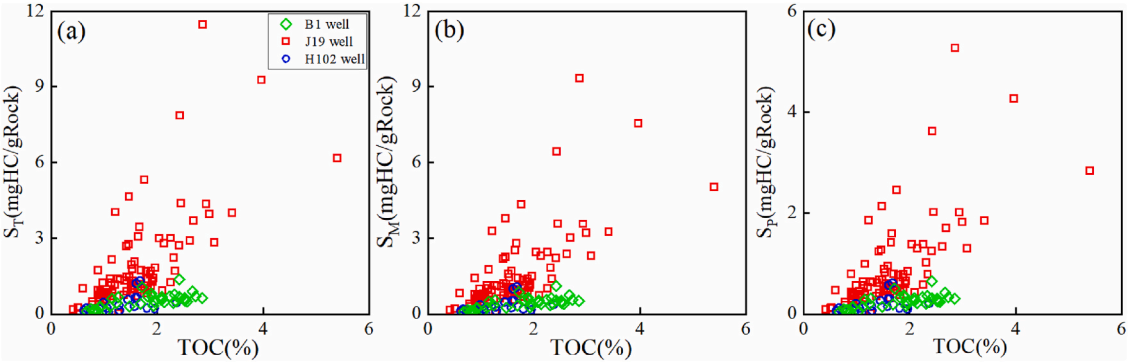

Fig. 15. Correlations between TOC and various oil content in the Second Mbr of the Funing Fm shale showing the increasing TOC bring about higher shale oil content: (a) plot of TOC vs S_T; (b) plot of TOC vs S_M; (c) plot of TOC vs S_E.

Funing Fm.

There are a large number of geochemical logging pyrolysis S_1 available to the Second Mbr of the Funing Fm in many wells, including C1, J7, J10, J20, J204 well. In addition, some measured pyrolysis S_1 data were also collected from the Second Mbr of the Funing Fm in the B1, Hl02, and J19 well. Based on pyrolysis S_1 collected from geochemical logging and measured samples, the light hydrocarbon recovery model and the oil content evaluation model are used to calculate the resulting S_T, S_M, and S_E. The well profile was established to investigate the variation of shale oil content in the Second Mbr of the Funing Fm. Overall, S_T, S_M, and S_E in the deep sag of the Qutang Sub-sag are the highest, and J19 and J204 wells in this zone show the highest S_T, S_M, and S_E values. Individual intervals in J10 and J20 wells show relatively high shale oil content, despite the shallow sag area having a low oil content background. The slopes of the Qutang Sub-sag and the Haibei Sub-sag contain the least shale oil, and S_T does not exceed 1.0 mgHC/gRock overall (Figs. 13 and 14). Vertically, oil content at the joint part of PSS4 and PSS5 is the best, followed by the ascending semi-cycle of PSS3, and the ascending semi-cycle of PSS2 in the J204 well also shows high oil content (Figs. 13 and 14).

5.3. *Controlling factors of shale oil content*

(1) Organic matter abundance

Organic matter is the material basis for hydrocarbon generation and determines the hydrocarbon-generating potential of source rocks. For source rocks with similar organic matter types in the oil window stage, the higher the organic matter abundance, the greater the amount of hydrocarbons generated. The TOC of the Second Mbr of the Funing Fm is typically less than 4% and has a positive correlation with oil content. S_T, S_M, and S_E continue to rise as TOC rises, with S_T showing the strongest upward trend (Fig. 15a–c). The correlation between TOC and shale oil content in different wells, on the other hand, is different. The oil content of J19 well in the deep sag area of the Qutang sub-sag increases significantly with the increase of TOC, whereas the oil content of H102 well in the slope of Qutang sub-sag and that of B1 well in Haibei sub-sag increases slightly, implying that TOC is not the only factor affecting oil content (Han et al., 2017). The deep sag area has better organic matter abundance and higher shale oil content.

(2) Thermal maturity

Thermal maturity has a significant impact on shale oil content and shale oil mobility. The Second Mbr of the Funing Fm has a wide range of burial depths, resulting in a great variation of thermal evolution degrees in different structural positions. However, the relationship between TOC and shale oil content in different wells is obviously different. The wells in the slope or shallow sag area, such as B1, C1, J7, J10, J20, and H102 wells, etc., have lower oil content, whereas those in the deep sag area, such as J19 and J204 wells, show higher oil content.

As the burial depth increases, OSI, S_T, and S_E first increase and then

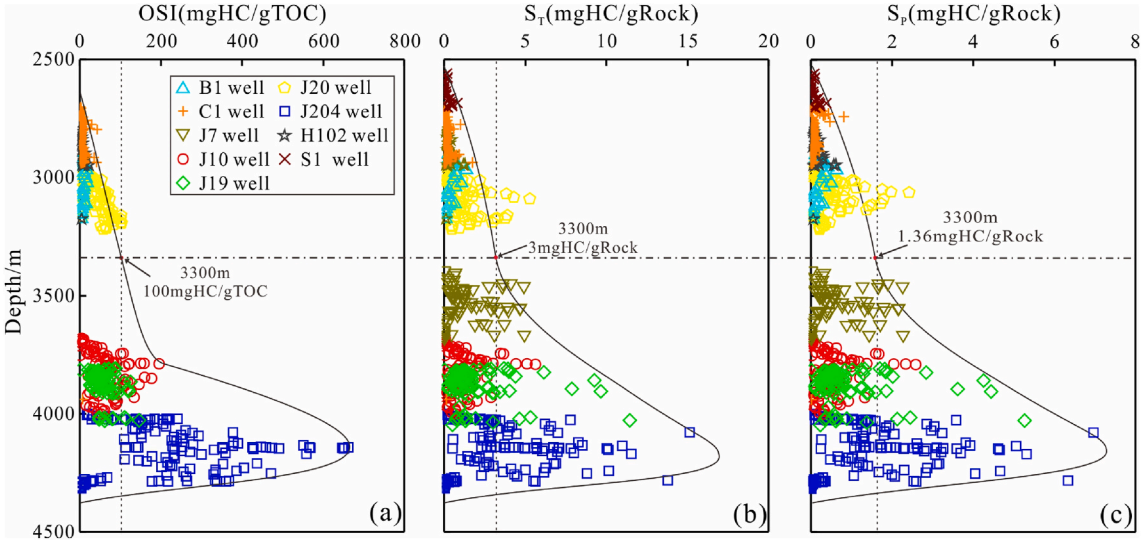

Fig. 16. Correlation between various oil content and depth for the Second Mbr of the Funing Fm showing that the first increase and then decrease in shale oil content with the increasing depth: (a) plot of OSI vs. Depth; (b) plot of S_T vs Depth; and (c) plot of S_P vs Depth.

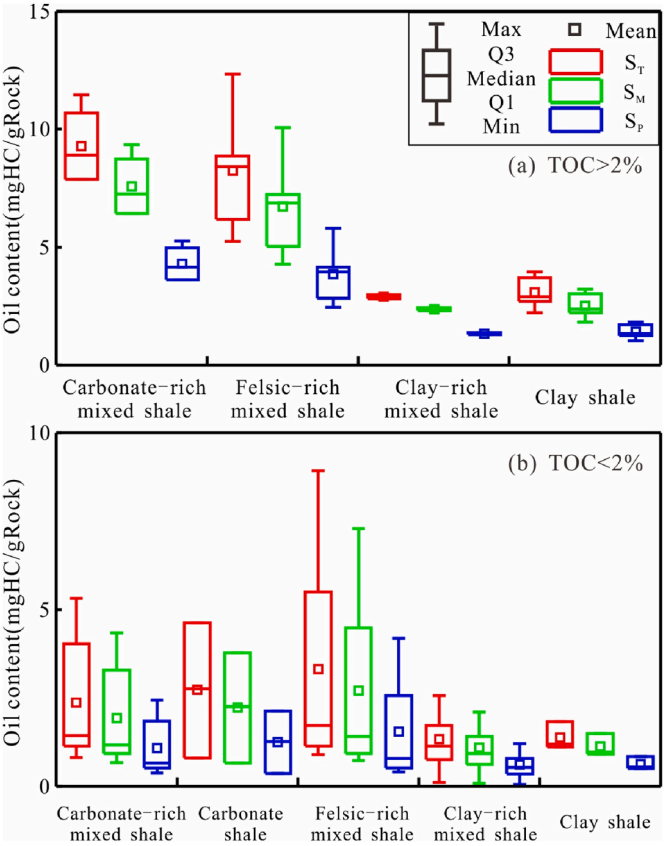

Fig. 17. Correlation between lithofacies determined by mineral compositions and various oil content for the Second Mbr of the Funing Fm showing that the increasing carbonate and felsic minerals in shales with similar TOC values bring about higher shale oil content: (a) box plot of lithofacies vs oil content for samples with TOC>2%; and (b) box plot of lithofacies vs oil content samples with TOC<2%.

decrease, and reach their maximum at about 4150 m, corresponding to an OSI of 650 mgHC/gTOC, S_T of 16 mgHC/gRock, and S_E of 6.97 mgHC/gRock, respectively (Fig. 16a–c). When buried depth exceeds 3300 m, OSI begins to exceed 100 mgHC/gTOC, indicating that 3300 m may be the depth boundary for the shale oil enrichment in the Second Mbr of the Funing Fm of the study area. When the burial depth exceeds 3300 m, shale oil in the Second Mbr of the Funing Fm begins to effectively accumulate and shows better production capacity, corresponding to S_T of 3 mgHC/gRock and S_E of 1.36 mgHC/gRock, respectively.

(3) Lithofacies determined by primary mineral compositions

The influence of mineral components on shale oil content can be attributed to differences in the wettability of clay and other types of minerals to hydrocarbon substances (Siddiqui et al., 2018), which result in differential adsorption and the occurrence of hydrocarbon compositions (Cao et al., 2021; Li et al., 2016b). This, in turn, affects shale oil mobility and local enrichment, resulting in variations in oil distribution across different types of shale lithofacies.

For shales with a TOC exceeding 2%, the carbonate-rich mixed shale has the highest S_T, S_M, and S_E, followed by the felsic-rich mixed shale. Low S_T, S_M, and S_E values are found in clay-rich mixed shale and clay shale (Fig. 17a). The carbonate-rich/felsic-rich mixed shale and carbonate shale have higher oil content than the clay-rich mixed clay shale and clay shale for shale with TOC less than 2%. (Fig. 17b). For shales possessing similar hydrocarbon generation potential and different lithofacies, the increasing content of felsic and carbonate minerals will generate better storage space for shale oil accumulation (Li et al., 2019), thus showing higher oil content in carbonate-rich and felsic-rich mixed shale than that in clay-rich mixed shale and clay shale.

(4) Sedimentary structure

The thin-section observation results show that the fluorescence characteristics in the laminated shale and the massive shale are significantly different (Fig. 18). The speckled fluorescence in the shale samples with laminae is distributed linearly along the laminated plane or locally concentrated (Fig. 18d), whereas the fluorescence in the massive

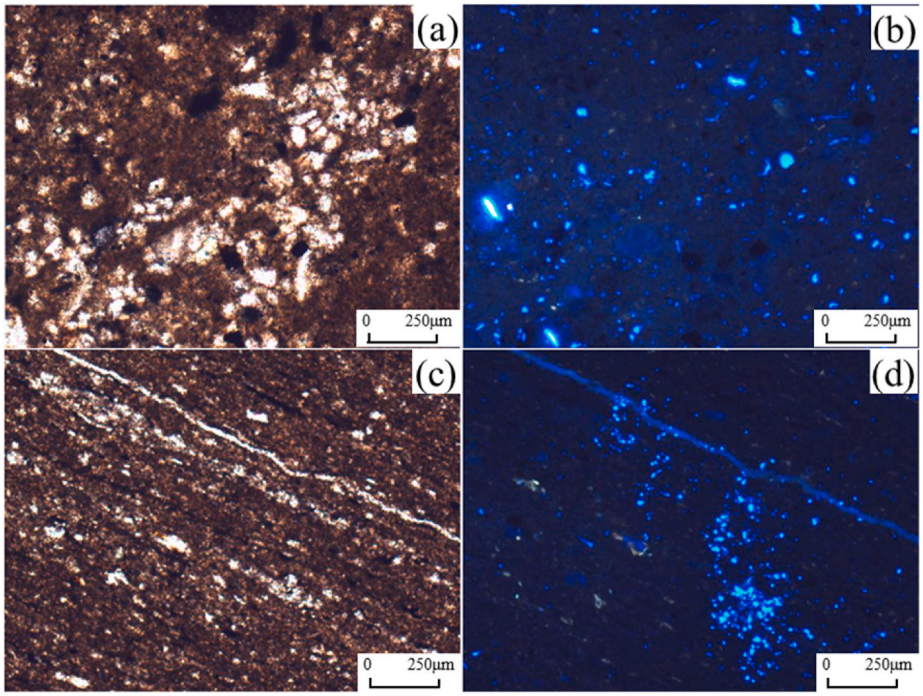

Fig. 18. Fluorescence thin sections under plane-polarized light and fluorescence light showing oil content characteristics of shales with different sedimentary structure: (a) and (b) J19 well, 3851.5 m, massive shale has dispersed organic matter and speckled fluorescence on the edge of coarse-grained light-colored minerals; (c) and (d) J19 well, 3906.5 m, laminated shale develops organic matter-clay-dolomite lamellae, and a microfracture is overall medium-light blue fluorescence, and spot-like fluorescence is locally concentrated on the edge of organic matter. (For interpretation of the references to color in this figure legend, the reader is referred to the Web version of this article.)

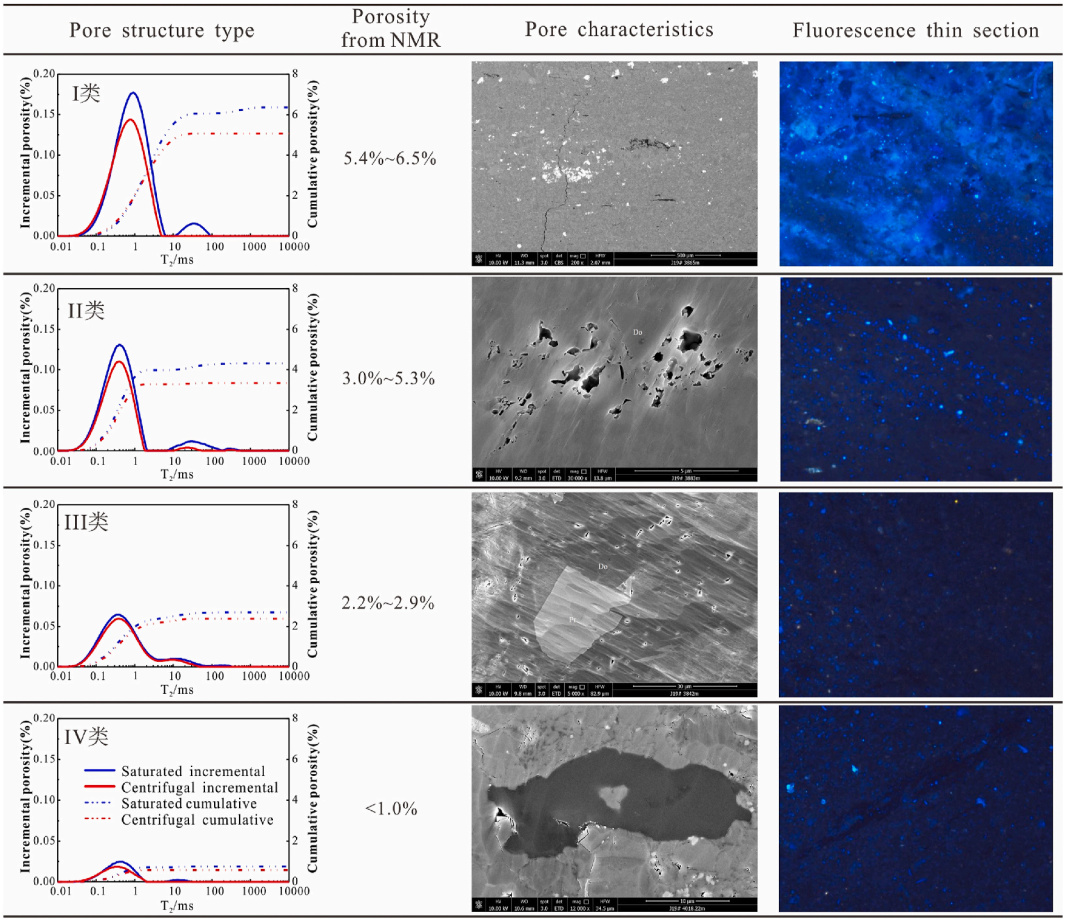

Fig. 19. Oil content characteristics of shales with different pore structures in Second Mbr of the Funing Fm based on T_2 spectra from NMR, SEM images, and thin-section images under fluorescence (after Liu et al. (2020)). I type pore structure shows a large T_2 amplitude difference and develops microfracture and matrix particle pores, and the framework grains emit bright blue fluorescence. II type pore structure has obvious T_2 amplitude difference and develops intercrystalline pores and particle dissolution pores, lamina emit light blue fluorescence. III type pore structure has low T_2 amplitude difference and develops organic pores, organic matter emits scattered dark blue fluorescence; IV type pore structure shows lowest T_2 amplitude difference and only has organic pores, rare fluorescence appear in framework grain. (For interpretation of the references to color in this figure legend, the reader is referred to the Web version of this article.)

shale is scattered in speckled features (Fig. 18b), demonstrating that the laminae play an important role in the local enrichment of shale oil. A large number of researchers have also confirmed that laminae in shale can greatly improve the permeability of shale reservoirs (Liu et al., 2019). The laminated structure is a key factor that needs to be considered in the selection of favorable reservoirs for lacustrine shale oil (Xi et al., 2020).

(5) Pore structure

Liu et al. (2020) identified four types of pore structure dependent on the T_2 spectra characteristics of the NMR in the Second Mbr of the Funing Fm, including I, II, III, and IV types (Fig. 19). Shale with type I of pore structure develops microfracture and matrix particle pores; shale with type II of pore structure develops intercrystalline pores and particle dissolution pores; shale with type III of pore structure develops organic matter pores, intraparticle dissolution pores, and interparticle pores; and shale with type IV of pore structure only has organic pores. The shales with type I and II pore structures show strong blue fluorescence in thin sections and good fluid mobility, owing to better reservoir quality, higher porosity of NMR test, better pore structure, more microfractures, and large pore size pores in these shales.

A detailed examination of the primary controlling factors of shale oil enrichment in the Second Mbr of the Funing Fm is summarized. The layer of shale oil enrichment is characterized by high TOC, high porosity, good pore structure, and high oil content and develops clay-rich mixed shale, felsic-rich mixed shale, and carbonate-rich mixed shale (Fig. 20). The intervals with laminated structures have the highest oil content. There is a good correlation between organic matter abundance and oil content, and high organic matter abundance often corresponds to high oil content. Carbonate-rich/felsic-rich mixed shale usually has better physical properties and pore structure than clay-rich mixed shale. Laminae can act as the flow channels of shale oil and play a key role in the local accumulation of shale oil (Xi et al., 2020). In addition, when the burial depth is 3300–4150 m, the shale oil is highly enriched and has a production capacity. The greater the burial depth in this range and the higher the thermal maturity, the higher the oil content.

6. Conclusion

The lacustrine shale oil content of the Second Mbr of the Funing Fm in Haian Sag (Subei Basin) was determined, the spatial occurrence of shale oil content was determined, and the primary controlling factors (TOC, thermal maturity, and lithofacies) of shale oil content were also defined.

A restoration model was developed for light hydrocarbon loss during drilling and coring, sample preservation, and sample pretreatment; the loss amount is greatest during sample preservation. The various petroleum groups are quantified by using chemical kinetics to decompose and

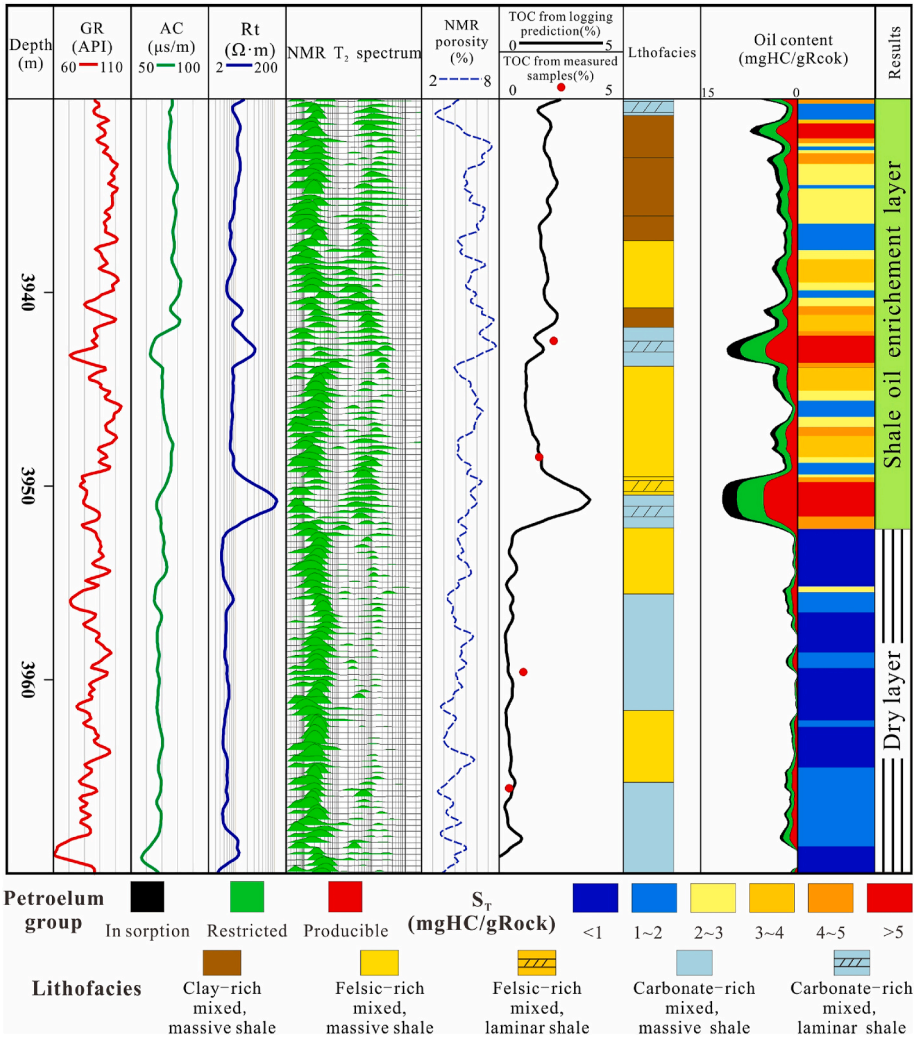

Fig. 20. Detailed evaluation of the controlling mechanism for oil heterogeneous distribution in the Second Mbr of the Funing Fm based on NMR T_2 spectra, NMR porosity, TOC, lithofacies, sedimentary structure, oil content showing that shale oil enrichment layers appear in carbonate-rich and felsic-rich mixed, laminated shales with better pore structure, higher porosity, higher TOC.

reconstruct FID pyrograms, and more accurate shale oil information is determined to reflect shale oil content and mobility. The total oil content, as a result, is approximately 3.55 times that of pyrolysis S_1.

TOC, thermal maturity, and lithofacies have a primary impact on the shale oil content. Shale oil in the Second Mbr of the Funing Fm prefers to accumulate in carbonate-rich and felsic-rich mixed, laminated shales with high TOC, high porosity, and good pore structure. This research provides effective parameters for prioritizing favorable shale oil exploration targets and calculating shale oil reserves in lacustrine shales with high heterogeneity, and it has implications for understanding oil accumulation and occurrence in shales with similar geological settings.

Funding

This work was supported by the National Natural Science Foundation of China [grant numbers 42072150 and 41372144] and the National Science and Technology Major Project of China [grant number 2017ZX05049001-008].

Declaration of competing interest

The authors declare that they have no known competing financial interests or personal relationships that could have appeared to influence the work reported in this paper.

Acknowledgements

We thank PetroChina Zhejing Oilfield Company and Wuxi Institute of Petroleum Geology, SINOPEC Exploration and Development Research Institute for their support. We appreciate the enthusiastic support of Prof. Zhuoheng Chen at Geological Survey of Canada, Menhui Qian at Wuxi Institute of Petroleum Geology, SINOPEC Exploration and Development Research Institute, and Yalan Yang at China University of Petroleum-Beijing. We acknowledge Prof. Hui Tian and two anonymous reviewers for their valuable comments and suggestions, which greatly improve the manuscript of an earlier version.

Appendix A. Supplementary data

Supplementary data to this article can be found online at https://doi.org/10.1016/j.marpetgeo.2021.105522.

References

Abrams, M.A., Gong, C., Garnier, C., Sephton, M.A., 2017. A new thermal extraction protocol to evaluate liquid rich unconventional oil in place and in-situ fluid chemistry. Mar. Petrol. Geol. 88, 659–675.

Beti, D.R., Jiang, C., Panja, P., Ring, T.A., Levey, R., 2020. Hydrocarbon distributions of incremental S1 peaks corresponding to different boiling point ranges of petroleum in

rock samples. J. Petrol. Sci. Eng. 191, 107174. https://10.1016/j.petrol.2020.107174.
Burnham, A.K., Braun, R.L., 1999. Global kinetic analysis of complex materials. Energy Fuel. 13 (1), 1–22. https://10.1021/ef9800765.
Cao, Z., Jiang, H., Zeng, J., Saibi, H., Lu, T., Xie, X., Zhang, Y., Zhou, G., Wu, K., Guo, J., 2021. Nanoscale liquid hydrocarbon adsorption on clay minerals: a molecular dynamics simulation of shale oils. Chem. Eng. J. 420, 127578. https://10.1016/j.cej.2020.127578.
Chen, J., Pang, X., Pang, H., Chen, Z., Jiang, C., 2018b. Hydrocarbon evaporative loss evaluation of lacustrine shale oil based on mass balance method: permian Lucaogou Formation in Jimusaer Depression, Junggar Basin. Mar. Petrol. Geol. 91, 422–431. https://10.1016/j.marpetgeo.2018.01.021.
Chen, S.P., Wang, X.Q., Wang, Z.Q., Qu, D.M., Luo, Y., 2009. The fracture Formation and its evolution from upper cretaceous to cenozoic in haian depression. Oil Geophys. Prospect. 44 (6), 760–766.
Chen, Z.H., Jiang, C.Q., 2020. An integrated mass balance approach for assessing hydrocarbon resources in a liquid-rich shale resource play: an example from upper Devonian Duvernay Formation, Western Canada sedimentary basin. J. Earth Sci. 31 (6), 1259–1272. https://10.1007/s12583-020-1088-1.
Chen, Z.H., Li, M., Cao, T., Ma, X., Li, Z., Jiang, Q., Li, Z., Jiang, C., 2017a. Hydrocarbon generation kinetics of a heterogeneous source rock system: example from the lacsutrine eocene-oligocene Shahejie formation, Bohai Bay basin, China. Energy Fuel. 31 (12), 13291–13304. https://10.1021/acs.energyfuels.7b02361.
Chen, Z.H., Li, M., Ma, X., Cao, T., Liu, X., Li, Z., Jiang, Q., Wu, S., 2018a. Generation kinetics based method for correcting effects of migrated oil on Rock-Eval data – an example from the Eocene Qianjiang Formation, Jianghan Basin, China. Int. J. Coal Geol. 195, 84–101.
Chen, Z.H., Li, M.W., Jiang, C.Q., Qian, M.H., 2019. Shale oil resource potential and its mobility assessment: a case study of Upper Devonian Duvernay shale in Western Canada Sedimentary Basin. Oil Gas Geol. 40 (3), 459–468. https://10.11743/ogg20190302.
Chen, Z.H., Liu, X., Guo, Q., Jiang, C., Mort, A., 2017b. Inversion of source rock hydrocarbon generation kinetics from Rock-Eval data. Fuel 194, 91–101. https://10.1016/j.fuel.2016.12.052.
di Primio, R., Horsfield, B., 2006. From petroleum-type organofacies to hydrocarbon phase prediction. AAPG (Am. Assoc. Pet. Geol.) Bull. 90 (7), 1031–1058. https://10.1306/02140605129.
Energy Information Administration, 2017. Major U.S. Tight Oil-Producing States Expected to Drive Production Gains through 2018. Available form: https://www.eia.gov/todayinenergy/detail.php? id=29752.
Gong, H.J., Li, Z.J., Zhu, C.F., Sang, Q., Li, Y.J., Dong, M.Z., 2020. Evaluating the content of movable oil in shale by technology of nuclear magnetic resonance. Res. Explor. Lab. 39 (2), 12–15, 2020.
Guan, M., 2021. The Oil Content Heterogeneity of Lacustrine Shale and its Controlling Mechanism in the Second Member of Funing Formation in Haian Sag. China University of Petroleum-Beijing, Beijing.
Han, K., Song, X., Yang, H., 2021. The pricing of shale gas: a review. J. Nat. Gas Sci. Eng. 89, 103897. https://10.1016/j.jngse.2021.103897.
Han, Y.J., Horsfield, B., Wirth, R., Mahlstedt, N., Bernard, S., 2017. Oil retention and porosity evolution in organic-rich shales. AAPG (Am. Assoc. Pet. Geol.) Bull. 101 (6), 807–827. http://10.1306/09221616069.
Hu, T., Pang, X., Jiang, S., Wang, Q., Zheng, X., Ding, X., Zhao, Y., Zhu, C., Li, H., 2018a. Oil content evaluation of lacustrine organic-rich shale with strong heterogeneity: a case study of the Middle Permian Lucaogou Formation in Jimusaer Sag, Junggar Basin, NW China. Fuel 221, 196–205. https://10.1016/j.fuel.2018.02.082.
Hu, W.Q., Ma, L.T., Liu, Y.M., Li, Y.B., Chen, X., Liu, X.Q., Wang, D., Ma, L.H., Liu, C., 2018b. Geochemical characteristics of hydrocarbon source rocks in Fu2 member of Qutang subsag, haian sag, Subei Basin. J. Northeast Petrol. Univ. 42 (5), 73–81.
Jarvie, D.M., 2012. Shale resource systems for oil and gas: Part 2— shale-oil resource systems. In: Breyer, J.A., Breyer, J.A. (Eds.), Giant Resources for the 21st Century, vol. 97. AAPG Memoir, pp. 89–119.
Jiang, C.Q., Chen, Z., Mort, A., Milovic, M., Robinson, R., Stewart, R., Lavoie, D., 2016b. Hydrocarbon evaporative loss from shale core samples as revealed by Rock-Eval and thermal desorption-gas chromatography analysis: its geochemical and geological implications. Mar. Petrol. Geol. 70, 294–303.
Jiang, C.Y., Jiang, W.Y., Zhou, N.F., 2018. Overall Evaluation and Development Plan of Tight Reservoir in the Source Area of Subei Exploration Area. Zhejiang Oilfield. Project Report, Hangzhou, pp. 1–146.
Jiang, Q.G., Li, M.W., Qian, M.H., Li, Z.M., Li, Z., Huang, Z.K., Zhang, C.M., Ma, Y.Y., 2016a. Quantitative characterization of shale oil in different occurrence states and its application. Petrol. Geol. Exp. 38 (6), 842–849. https://10.11781/sysydz201606842.
Jin, Z.J., Bai, Z.H., Gao, B., Li, M.W., 2019. Has China ushered in the shale oil and gas revolution? Oil Gas Geol. 40 (3), 451–458.
Lazar, O.R., Bohacs, K.M., Macquaker, J.H.S., Schieber, J., Demko, T.M., 2015. Capturing key attributes of fine-grained sedimentary rocks in outcrops, cores, and thin sections: nomenclature and description guidelines. J. Sediment. Res. 85 (3), 230–246. https://10.2110/jsr.2015.11.
Li, B.Y., Pang, X., Dong, Y., Peng, J., Gao, P., Wu, H., Huang, C., Shao, X., 2019. Lithofacies and pore characterization in an argillaceous-siliceous-calcareous shale system: a case study of the Shahejie Formation in Nanpu sag, Bohai Bay basin, China. J. Petrol. Sci. Eng. 173, 804–819. https://doi.org/10.1016/j.petrol.2018.10.086.
Li, H., Lu, J.L., Wang, B.H., Song, Z.X., Li, Z., 2020b. Critical controlling factors of enrichment and high-yield of land shale oil. Geoscience 34 (4), 837–848. https://10.19657/j.geoscience.1000-8527.2020.04.19.
Li, J., Jiang, C., Wang, M., Lu, S., Chen, Z., Chen, G., Li, J., Li, Z., Lu, S., 2020d. Adsorbed and free hydrocarbons in unconventional shale reservoir: a new insight from NMR T1-T2 maps. Mar. Petrol. Geol. 116, 104311. https://10.1016/j.marpetgeo.2020.104311.
Li, J.B., Lu, S.F., Xie, L., Zhang, J., Xue, H., Zhang, P., Tian, S., 2017. Modeling of hydrocarbon adsorption on continental oil shale: a case study on n-alkane. Fuel 206, 603–613. https://10.1016/j.fuel.2017.06.017.
Li, M.W., Chen, Z., Ma, X., Cao, T., Li, Z., Jiang, Q., 2018. A numerical method for calculating total oil yield using a single routine Rock-Eval program: a case study of the Eocene Shahejie Formation in Dongying Depression, Bohai Bay Basin, China. Int. J. Coal Geol. 191, 49–65.
Li, M.W., Chen, Z.H., Qian, M.H., Ma, X., Jiang, Q., Li, Z., Tao, G., Wu, S., 2020c. What are in pyrolysis S1 peak and what are missed? Petroleum compositional characteristics revealed from programed pyrolysis and implications for shale oil mobility and resource potential. Int. J. Coal Geol. 217, 103321.
Li, M.W., Jin, Z.J., Dong, M.Z., Ma, X.X., Li, Z.M., Jiang, Q.G., Bao, Y.J., Tao, G.L., Liu, P., Cao, T.T., 2020a. Advances in the basic study of lacustrine shale evolution and shale oil accumulation. Petrol. Geol. Exp. 42 (4), 489–505. https://10.11781/sysydz202004489.
Li, S., Hu, S., Xie, X., Lv, Q., Huang, X., Ye, J., 2016a. Assessment of shale oil potential using a new free hydrocarbon index. Int. J. Coal Geol. 156, 74–85. https://10.1016/j.coal.2016.02.005.
Li, W., Lu, S., Xue, H., Zhang, P., Hu, Y., 2015. Oil content in argillaceous dolomite from the Jianghan Basin, China: application of new grading evaluation criteria to study shale oil potential. Fuel 143, 424–429. https://10.1016/j.fuel.2014.11.080.
Li, Z., Zou, Y., Xu, X., Sun, J., Li, M., Peng, P.A., 2016b. Adsorption of mudstone source rock for shale oil–Experiments, model and a case study. Org. Geochem. 92, 55–62. https://10.1016/j.orggeochem.2015.12.009.
Liu, D., Li, Z., Jiang, Z., Zhang, C., Zhang, Z., Wang, J., Yang, D., Song, Y., Luo, Q., 2019. Impact of laminae on pore structures of lacustrine shales in the southern Songliao Basin, NE China. J. Asian Earth Sci. 182, 103935. https://10.1016/j.jseaes.2019.103935.
Liu, X., Lai, J., Fan, X., Shu, H., Wang, G., Ma, X., Liu, M., Guan, M., Luo, Y., 2020. Insights in the pore structure, fluid mobility and oiliness in oil shales of Paleogene Funing Formation in Subei Basin, China. Mar. Petrol. Geol. 114, 104228.
Liu, Y., Zeng, J., Yang, G., Jia, W., Liu, S., Kong, X., Li, S., 2021. An innovative method for the characterization of oil content in lacustrine shale-oil systems: a case study from the Middle Permian Lucaogou Formation in the Jimusaer Sag, Junggar Basin. Mar. Petrol. Geol. 130, 105112. https://10.1016/j.marpetgeo.2021.105112.
Lu, S.F., Huang, W.B., Chen, F.W., Li, J.J., Wang, M., Xue, H.T., Wang, W.M., Cai, X.Y., 2012. Classification and evaluation criteria of shale oil and gas resources: discussion and application. Petrol. Explor. Dev. 39 (2), 249–256.
Michael, G.E., Packwood, J., Holba, A., 2013. Determination of in-situ hydrocarbon volumes in liquid-rich shale plays. In: Unconventional Resources Technology Conference. AAPG, Vancouver, BC, Canada.
Nikolaev, M.Y., Kazak, A.V., 2019. Liquid saturation evaluation in organic-rich unconventional reservoirs: a comprehensive review. Earth Sci. Rev. 194, 327–349. https://10.1016/j.earscirev.2019.05.012.
Penner, S.S., 1952. On the kinetics of evaporation. J. Phys. Chem. 56 (4), 475–479.
Qian, M.H., Li, M.W., Jiang, Q.G., Li, Z.M., Tao, G.L., Bao, Y.J., 2019. Hydrocarbon loss characteristics of shale samples and its geological significance. In: National Conference on Organic Geochemistry. Fuzhou.
Ran, H.J., Si, B.L., Chen, F.H., Fan, L.Y., 2012. Sedimentary sequences in haian depression and control on reservoir of the paleocene. Oil Geophys. Prospect. 47 (5), 795–802.
Romero-Sarmiento, M., 2019. A quick analytical approach to estimate both free versus sorbed hydrocarbon contents in liquid-rich source rocks. AAPG (Am. Assoc. Pet. Geol.) Bull. 103 (9), 2031–2043.
Romero-Sarmiento, M., Pillot, D., Letort, G., Lamoureux-Var, V., Beaumont, V., Huc, A., Garcia, B., 2016. New rock-eval method for characterization of unconventional shale resource systems. Oil Gas Sci. Technol. Revue d' IFP Energy Nouv. 71 (3), 37.
Sang, Q., Zhang, S., Li, Y., Dong, M., Bryant, S., 2018. Determination of organic and inorganic hydrocarbon saturations and effective porosities in shale using vacuum-imbibition method. Int. J. Coal Geol. 200, 123–134. https://10.1016/j.coal.2018.10.010.
Shu, L.S., Wang, B., Wang, L.S., He, G.Y., 2005. Analysis of northern Jiangsu prototype basin from late cretaceous to Neogene. Geol. J. China Univ. 11 (4), 534–543.
Siddiqui, M.A.Q., Ali, S., Fei, H., Roshan, H., 2018. Current understanding of shale wettability: a review on contact angle measurements. Earth Sci. Rev. 181, 1–11. https://10.1016/j.earscirev.2018.04.002.
Soeder, D.J., 2018. The successful development of gas and oil resources from shales in North America. J. Petrol. Sci. Eng. 163, 399–420. https://10.1016/j.petrol.2017.12.084.
Sui, H., Zhang, F., Wang, Z., Wang, D., Wang, Y., 2020. Molecular simulations of oil adsorption and transport behavior in inorganic shale. J. Mol. Liq. 305, 112745. https://10.1016/j.molliq.2020.112745.
Wang, Z.Q., Li, H.D., Du, E.P., 2012. Features of present structural stress field and structural pattern in Haian Depression, Northern Jiangsu Basin. J. Geomechanics 18 (1), 22–31. https://10.3969/j.issn.1006-6616.2012.01.003.
Wang, J., 2015. Low-temperature closed extraction technology of light hydrocarbons and its application in evaluation of shale oil resource. Chin. Petrol. Explor. 20 (3), 58–63, 2015.
Wang, M., Guo, Z., Jiao, C., Lu, S., Li, J., Xue, H., Li, J., Li, J., Chen, G., 2019. Exploration progress and geochemical features of lacustrine shale oils in China. J. Petrol. Sci. Eng. 178, 975–986.

Wang, S., Feng, Q.H., Javadpour, F., Xia, T., Li, Z., 2015. Oil adsorption in shale nanopores and its effect on recoverable oil-in-place. Int. J. Coal Geol. 147–148, 9–24. https://10.1016/j.coal.2015.06.002.

Xi, K.L., Li, K., Cao, Y.C., Lin, M.R., Niu, X.B., Zhu, R.K., Wei, X.Z., You, Y., Liang, X.W., Feng, S.B., 2020. Laminae combination and shale oil enrichment patterns of Chang 73 sub-member organic-rich shales in the Triassic Yanchang Formation, Ordos Basin, NW China. Petrol. Explor. Dev. 47 (6), 1244–1255. https://10.11698/PED.2020.06.18.

Xue, H.T., Tian, S.S., Wang, W.M., Zhang, W.H., Du, T.T., Mu, G.D., 2016. Correction of oil content—one key parameter in shale oil resource assessment. Oil Gas Geol. 37 (1), 15–22. https://10.11743/ogg20160103.

Zhang, H., Huang, H., Li, Z., Liu, M., 2020. Comparative study between sequential solvent-extraction and multiple isothermal stages pyrolysis: a case study on Eocene Shahejie Formation shales, Dongying Depression, East China. Fuel 263, 116591. https://10.1016/j.fuel.2019.116591.

Zhang, J.C., Lin, L.M., Li, Y.X., Tang, X., Zhu, L.L., Xing, Y.W., Yang, S.Y., 2012. Classification and evaluation of shale oil. Earth Sci. Front. 19 (5), 322–331.

Zhang, L.Y., Bao, Y.S., Li, J.Y., Li, Z., Zhu, R.F., Zhang, J.G., 2014. Movability of lacustrine shale oil: a case study of dongying sag, Jiyang depression, Bohai Bay basin. Petrol. Explor. Dev. 41 (6), 641–649. https://10.11698/PED.2014.06.01.

Zhu, C., Guo, W., Li, Y., Gong, H., Sheng, J.J., Dong, M., 2021. Effect of occurrence states of fluid and pore structures on shale oil movability. Fuel 288, 119847. https://10.1016/j.fuel.2020.119847.

Zink, K.G., Scheeder, G., Stueck, H.L., Biermann, S., Blumenberg, M., 2016. Total shale oil inventory from an extended Rock-Eval approach on non-extracted and extracted source rocks from Germany. Int. J. Coal Geol. 163, 186–194. https://10.1016/j.coal.2016.06.023.

Zou, C., Zhu, R., Chen, Z., Ogg, J.G., Wu, S., Dong, D., Qiu, Z., Wang, Y., Wang, L., Lin, S., Cui, J., Su, L., Yang, Z., 2019. Organic-matter-rich shales of China. Earth Sci. Rev. 189, 51–78.